PCCP

ROYAL SOCIETY OF CHEMISTRY

PAPER

View Article Online
View Journal | View Issue

Check for updates

Cite this: *Phys. Chem. Chem. Phys.*, 2025, **27**, 20885

Exploring $Cs_2AgIn_xBi_{1-x}Cl_6$ double perovskites for optoelectronics: insights from theoretical and photophysical approaches

Swati N. Rahane,[a] Ganesh K. Rahane,[b] Yogesh Jadhav,[c] Mamta P. Nasane,[d] Henry I. Eya,[f] Deepak Kalleshappa,[d] K. Hareesh,[b] Jayant Pawar,[e] Sandesh R. Jadkar*[a] and Nelson Y. Dzade*[f]

Lead-free halide double perovskites (HDPs) have become attractive materials for optoelectronic applications owing to their nontoxicity, structural stability, and germane photoelectric properties. In this work, we report the synthesis of high-quality In-alloyed $Cs_2AgIn_xBi_{1-x}Cl_6$ nanocrystals (NCs) using the antisolvent recrystallization method and comprehensively investigate the effects of In alloying on the structural, morphological, optoelectronic, and temperature-dependent photoluminescence (TDPL) properties using the state-of-the-art experimental and computational tools. Both XRD and Raman spectroscopy analyses confirmed the synthesis of highly crystalline $Cs_2AgIn_xBi_{1-x}Cl_6$ materials, which exhibited cubic morphology, as confirmed by TEM analysis. Room-temperature photoluminescence (PL) measurements revealed a drastic increase in the intensity above 75% In concentration with dual emission, whereas the time-resolved PL (TR-PL) results show an increase in the average lifetime values with an increase in In content, suggesting that the materials have excellent optical properties and hence are suitable candidates for optoelectronics. The TDPL measurements revealed the smallest Huang–Rhys factor (18.6) for the $Cs_2AgIn_xBi_{(1-x)}Cl_6$ (x = 0.9) sample, indicating weak exciton–phonon coupling in this composition. When deployed in the fabrication of a photodetector device, the $Cs_2AgIn_xBi_{(1-x)}Cl_6$ (x = 0.9) sample exhibited significantly enhanced photoresponsivity and a faster response time, confirming its potential for photodetector applications. Complementary DFT calculations showed that In alloying modifies the band structure of $Cs_2AgIn_xBi_{(1-x)}Cl_6$. Our results provide valuable insights for designing multifunctional $Cs_2AgIn_xBi_{(1-x)}Cl_6$-based materials for next-generation energy and optoelectronic devices.

Received 13th June 2025,
Accepted 30th August 2025

DOI: 10.1039/d5cp02259b

rsc.li/pccp

Open Access Article. Published on 04 September 2025. Downloaded on 1/29/2026 4:49:33 AM.
This article is licensed under a Creative Commons Attribution 3.0 Unported Licence.

1. Introduction

Metal halide perovskites (MHPs) have emerged as a promising class of perovskites for cost-effective and high-performance applications in solar cells, light-emitting diodes (LEDs), and displays.[1–3] These perovskites demonstrate high optical absorption coefficients, significant PL quantum yields (PLQYs), and easily tunable band gaps.[4–10] Moreover, they possess higher carrier lifetimes and diffusion lengths of charge carriers.[11,12] Such significant attributes render halide perovskites highly intriguing and suggest potential superiority over traditional optoelectronic devices. Their superior performance is primarily ascribed to their direct band gap and three-dimensional (3D) structure.[13] Altering the dimensions of MHPs from 3D to zero-dimensional (0D) by adjusting the A-site cation's size is feasible. However, the lower-dimensional perovskites currently trail behind their 3D counterparts in solar cell applications due to their limited light-harvesting capabilities.[14,15]

Understanding the optical properties and band structure of a semiconductor is vital for designing and developing efficient optoelectronic devices, as the band gap directly determines a material's ability to absorb and emit light, influencing the overall functionality of these devices. Recent studies have focused on all-inorganic lead halide perovskite nanocrystals ($CsPbX_3$, X = Cl, Br, I). These perovskites possess a unique three-dimensional structure and a direct band gap, resulting in

[a] *Department of Physics, Savitribai Phule Pune University, Pune 411007, India. E-mail: sandesh@physics.unipune.ac.in*
[b] *Department of Physics, Manipal Institute of Technology Bengaluru, Manipal Academy of Higher Education, Manipal 576104, India*
[c] *BacPlexTechnologies Private Limited, C/O AIC IISER Pune Seed Foundation, IISER Pune Campus, Dr Homi Bhabha Road, Pashan, Pune 411008, Maharashtra, India*
[d] *Department of Physics, School of Applied Sciences, REVA University, Yelahanka, Bengaluru, Karnataka, 560064, India*
[e] *Krishna Vishwa Vidyapeeth (Deemed to be University), Malkapur, Karad-415539, Maharashtra, India*
[f] *Department of Energy and Mineral Engineering, Pennsylvania State University, University Park, PA 16802, USA. E-mail: nxd5313@psu.edu*

Open Access Article. Published on 04 September 2025. Downloaded on 1/29/2026 4:49:33 AM. This article is licensed under a Creative Commons Attribution 3.0 Unported Licence.

a high absorption coefficient, low trap-state density, and near-unity photoluminescence quantum efficiency (PLQE), which makes them promising for optoelectronic applications.[16–19] Despite their promising attributes, lead halide perovskites face toxicity and stability issues. Efforts have been made to develop lead-free alternatives with exceptional environmental stability. In this perspective, some progress has been made with Bi^{3+}, Sb^{3+}, and DP NCs.[20–30] These lead-free perovskites show an indirect band gap, leading to lower performance.

Recently, a novel lead-free $Cs_2AgInCl_6$ double perovskite (DP) possessing a band gap of 3.5 eV has been introduced.[31–34] This material features a direct band gap, with absorption occurring between the ultraviolet (UV) and visible regions.[31] In contrast, $Cs_2AgBiCl_6$ exhibits an indirect band gap of approximately 2.7–2.8 eV. Essentially, $Cs_2AgInCl_6$ demonstrates a direct transition with a wider band gap, while $Cs_2AgBiCl_6$ showcases an indirect transition with a relatively narrower band gap.[35] Designing DP systems to converge indirect-to-direct transitions by adjusting the composition could yield materials with intermediate band gaps and enhanced optical properties, making them attractive for a wide range of applications. These multifunctional properties have recently sparked interest in semiconductors for more versatile high-performance optoelectronic applications.[36–38]

While the optical properties have been studied in detail for the end members of the $Cs_2AgIn_xBi_{1-x}Cl_6$ family through TDPL measurements, other important properties like intrinsic defects, self-trapping, recombination rates, and the applications in the field of optoelectronics have not been thoroughly studied for the compositional materials. A comprehensive approach combining experimental techniques, DFT, and advanced characterizations is essential to understand better the physical processes, such as defect states and band gap tunability. In this study, we systematically investigated $Cs_2AgIn_xBi_{(1-x)}Cl_6$ materials to determine the impact of chemical changes on the structural, optical, and electronic properties of these DP materials. Raman spectroscopy analysis provides insights into the local distortions, as well as the active vibrational modes present in the materials. These highly stable DPs exhibit emission in the visible region, which may be related to defect levels and surface traps. X-ray diffraction (XRD) analysis verified that all synthesized materials crystallize in the cubic phase. Energy dispersive spectroscopy (EDS) results indicated a proportional increase in the atomic composition of In with an increase in In content, consistent with stoichiometry. We employed TDPL to probe the excitonic and defect states, and electrochemistry to assess charge transport. As the energy band alignment and band offset control charge transport and separation across the perovskite interface, we employed electrochemical cyclic voltammetry (CV) measurements to determine the band edge positions, specifically the valence band maximum (VBM) and the conduction band minimum (CBM). The results showed prominent peaks, which are correlated with electron transfer from the valence band to the conduction band edge. Additionally, first-principles DFT calculations were used to gain insights into the electronic structure of these DPs. Beyond fundamental understanding, we demonstrate the potential of these materials for photodetector applications. This multidisciplinary approach not only advances our understanding of perovskite materials but also provides strategic insights for optimizing their functionality in real-world applications. These materials hold significant promise for applications in optoelectronics as well as photocatalysis, making them strong candidates for advancements in these fields.

2. Experimental section/methods

2.1 Materials

CsCl (TCI, 99%), AgCl (Sigma-Aldrich 99.99%), $BiCl_3$ (HPLC, 92%), $InCl_3$ (TCI, 99.99%), isopropanol (IPA, AR grade, 99.5%), dimethyl sulfoxide (DMSO, AR grade, 99.5%), tetrabutylammonium perchlorate (TBAP-99.8%), and toluene (AR grade, HPLC, 99.5%) were used directly as received.

2.2 Synthesis of $Cs_2AgIn_xBi_{1-x}X_6$ (x = 0, 0.1, 0.25, 0.5, 0.75, 0.9, 1.0)

To synthesize the $Cs_2AgIn_xBi_{1-x}Cl_6$ (x = 0) NCs, CsCl, AgCl, and $BiCl_3$ metal salts were dissolved in DMSO in a ratio of 2 : 1 : 1 to form a precursor solution. Typically, 0.2 mmol CsCl (33.7 mg), 0.1 mmol AgCl (14.3 mg), and 0.1 mmol $BiCl_3$ (31.5 mg) were dissolved in 5 mL DMSO to prepare the precursor solution. Next, 100 μL of this solution was added dropwise into 5 mL of IPA with vigorous stirring. The resulting solution was then centrifuged at 4500 rpm for 5 minutes to remove large crystals, and the obtained product was washed three times to eliminate byproducts. The synthesis procedure for $Cs_2AgIn_xBi_{1-x}Cl_6$ (x = 1) NCs was similar to that of $Cs_2AgIn_xBi_{1-x}Cl_6$ (x = 0) NCs. For $Cs_2AgIn_xBi_{1-x}Cl_6$ (x = 1) NCs, 0.2 mmol CsCl, 0.1 mmol AgCl, and 0.1 mmol $InCl_3$ were mixed in 5 mL DMSO to prepare the precursor solution, followed by dropwise addition of 100 μL of the precursor solution into 5 mL of IPA under vigorous stirring. This solution was centrifuged at 4500 rpm for 5 minutes and washed subsequently. A similar approach was employed for synthesizing $Cs_2AgIn_xBi_{1-x}X_6$ (x = 0, 0.10, 0.25, 0.50, 0.75, 0.90, 1.0) NCs, with varying amounts of CsCl, AgCl, $BiCl_3$, and $InCl_3$ used to form precursors for injection.

2.3 Fabrication of the photodetector device

Fluorine-doped tin oxide (FTO) was used as the substrate for fabricating the photodetector device. Initially, the substrates were cleaned by sequential sonication in isopropyl alcohol, double-distilled water, and acetone for 15 minutes each. Following the cleaning process, a compact TiO_2 (c-TiO_2) layer was deposited onto the FTO substrates using radiofrequency (RF) sputtering, serving as the electron transport layer (ETL). Subsequently, the active material was deposited onto the TiO_2-coated FTO substrate *via* a simple drop-casting method. Finally, the cathode contact was given using graphite paste to form an FTO/c-TiO_2/$Cs_2AgIn_xBi_{(1-x)}Cl_6$/graphite photodetector device. For the top electrode contact, a graphite paste was prepared

 This journal is © the Owner Societies 2025

Open Access Article. Published on 04 September 2025. Downloaded on 1/29/2026 4:49:33 AM. This article is licensed under a Creative Commons Attribution 3.0 Unported Licence.

by mixing graphite powder in an IPA solution, and then it was deposited on FTO/c-TiO_2/$Cs_2AgIn_xBi_{(1-x)}Cl_6$.

2.4 Characterization of $Cs_2AgIn_xBi_{1-x}Cl_6$

XRD analysis was carried out utilizing a Bruker HR-XRD D8 Advance instrument with Cu-Kα radiation at 1.542 Å to obtain diffraction patterns. Raman measurements were performed using a Renishaw inVia Raman microscope. An excitation wavelength of 532 nm was used as the source. UV/visible spectra were collected in DRS mode using a JASCO V-670 UV-visible spectrophotometer. High-resolution imaging was performed using aberration-corrected TEM in HR-TEM mode (Thermo Fisher Tecnai T-20 ST) operating at 200 kV. The surface morphology and shape of the $Cs_2AgIn_xBi_{(1-x)}Cl_6$ DPs were examined through FE-SEM. Compositional analysis was conducted using EDS with a Bruker X Flash 6130 instrument. A PHI 5000 VERSA PROBE III ULVAC PHI instrument (Physical Electronics, USA) was used for XPS employing monochromatic AlK_α radiation at 1486.6 eV. The XPS chamber maintained a base vacuum level above 10^{-9} torr. Room temperature PL was conducted utilizing a Fluorolog Horiba scientific setup, while the TDPL measurements employed a JANIS (model no. VNF-10) PL setup. Time-resolved photoluminescence (TRPL) was conducted using a Horiba Jobin Yvon FluoroCube-01-NL fluorescence lifetime system, equipped with a 405 nm picosecond laser diode source that can generate pulse widths shorter than 70 ps. Data analysis was carried out using Horiba DataStation software. A Metrohm Potentiostat/Galvanostat Autolab PGSTAT 302N was employed for CV measurements. A standard three-electrode system was used to record CV curves as per our previous report.[39–42] A glassy carbon electrode was used as the working electrode, and a silver wire and platinum were used as the reference and counter electrodes, respectively. The measurements were performed in a 15 mL solution of dichloromethane (DCM) containing 100 mM tetrabutylammonium perchlorate (TBAP) as the supporting electrolyte, all under inert nitrogen conditions. Before conducting CV measurements, the glassy carbon electrode was polished using alumina powder (0.5 μm), while the Ag/Pt electrodes were cleaned with dilute nitric acid and then rinsed with deionized water. Photoresponse measurements of the $Cs_2AgIn_xBi_{(1-x)}Cl_6$ double perovskite devices were recorded using a Keithley 2450 source meter connected to a computer. Light illumination was incident through an ORIEL SOL 2A 94022A Class ABA simulator. *I–V* characteristics were measured at a power density of 30 mW cm^{-2} on an active layer with an area of 1.5 × 1.5 cm^2.

2.5 First-principles DFT characterization

The first-principles DFT calculations were performed using the Vienna *Ab initio* Simulation Package (VASP).[43] First, we obtained the crystallographic files (CIFs) of $Cs_2AgIn_xBi_{(1-x)}Cl_6$ (x = 0) and $Cs_2AgIn_xBi_{(1-x)}Cl_6$ (x = 1) from the Materials Project database and performed geometric optimization using the generalized gradient approximation (GGA) Perdew–Burke–Ernzerhof (PBE) functional.[44] The ion core and valence electron wavefunctions were described using the projector augmented wavefunction (PAW) pseudopotentials,[45] and a plane-wave energy cut-off of 600 eV was employed to converge the total energy of the structures within 10^{-7} eV and the residual forces on all relaxed atoms to 10^{-3} eV $Å^{-1}$. The Brillouin zone was sampled using a 3 × 3 × 3 Monkhorst–Pack k-point mesh.[46] Furthermore, we accounted for vdW interactions in our calculations using the Grimme (DFT-D3) method.[47] Considering that the PBE functional underestimates the band gap of semiconductors, we employed the Hartree–Fock screened hybrid functional (HSE06) for the electronic and optical property calculations. Hartree–Fock exchange fractions of 25% and 40% were employed for $Cs_2AgIn_xBi_{(1-x)}Cl_6$ (x = 0) and $Cs_2AgIn_xBi_{(1-x)}Cl_6$ (x = 1), respectively, as they could predict the band gaps of the respective materials close to their experimental values. A higher k-point mesh of 5 × 5 × 5 was used for the density of states (DOS) and optical property calculations. The projected density of states (PDOS) and band structures were plotted using SUMO software.[48] The linear optical properties of the materials were determined from the frequency-dependent complex dielectric function $\varepsilon(w)$, which is expressed as follows:

$$\varepsilon(w) = \varepsilon_1(w) + i\varepsilon_2(w), \quad (1)$$

where $\varepsilon_1(w)$ and $\varepsilon_2(w)$ are the real and imaginary parts of the dielectric function, respectively, and w is the photon frequency. The frequency-dependent linear optical spectra, including the absorption coefficient $\alpha(w)$, refractive index $n(w)$, and reflectivity $R(w)$, were obtained from $\varepsilon_1(w)$ and $\varepsilon_2(w)$ as follows:[49,50]

$$\alpha(w) = \frac{\sqrt{2}w}{c}\left[\sqrt{\varepsilon_1^2 + \varepsilon_2^2} - \varepsilon_1\right]^{\frac{1}{2}} \quad (2)$$

$$n(w) = \left[\frac{\sqrt{\varepsilon_1^2 + \varepsilon_2^2} + \varepsilon_1}{2}\right]^{\frac{1}{2}} \quad (3)$$

$$R(w) = \frac{(n-1)^2 + k^2}{(n+1)^2 + k^2} \quad (4)$$

where c is the speed of light in a vacuum. These optical properties were extracted using VASPKIT.[49]

3. Results and discussion

3.1 Structural properties of $Cs_2AgIn_xBi_{1-x}Cl_6$ DPs

3.1.1 XRD analysis. The $Cs_2AgIn_xBi_{1-x}Cl_6$ (x = 0.0, 0.1, 0.25, 0.5, 0.75, 0.9, 1.0) NCs were synthesized *via* the antisolvent recrystallization method.[25,28] The stoichiometry of In/Bi was varied to prepare the In-alloyed $Cs_2AgIn_xBi_{1-x}Cl_6$ NCs. The XRD patterns of all these DPs are shown in Fig. 1(a). XRD analysis confirmed the high crystallinity of the synthesized materials, with all NCs adopting the $Fm\bar{3}m$ cubic space group like $Cs_2AgIn_xBi_{1-x}Cl_6$ (x = 0) DPs.[28] We observe a monotonic shift in XRD peaks towards higher angles with an increase in In content, as can be seen for the peak at around 34° (Fig. 1(b)), indicating lattice contraction due to the replacement of larger Bi^{3+} (ionic radius = 117 pm) with the smaller In^{3+} (94 pm). Fig. S1 in the SI

Open Access Article. Published on 04 September 2025. Downloaded on 1/29/2026 4:49:33 AM.
This article is licensed under a Creative Commons Attribution 3.0 Unported Licence.

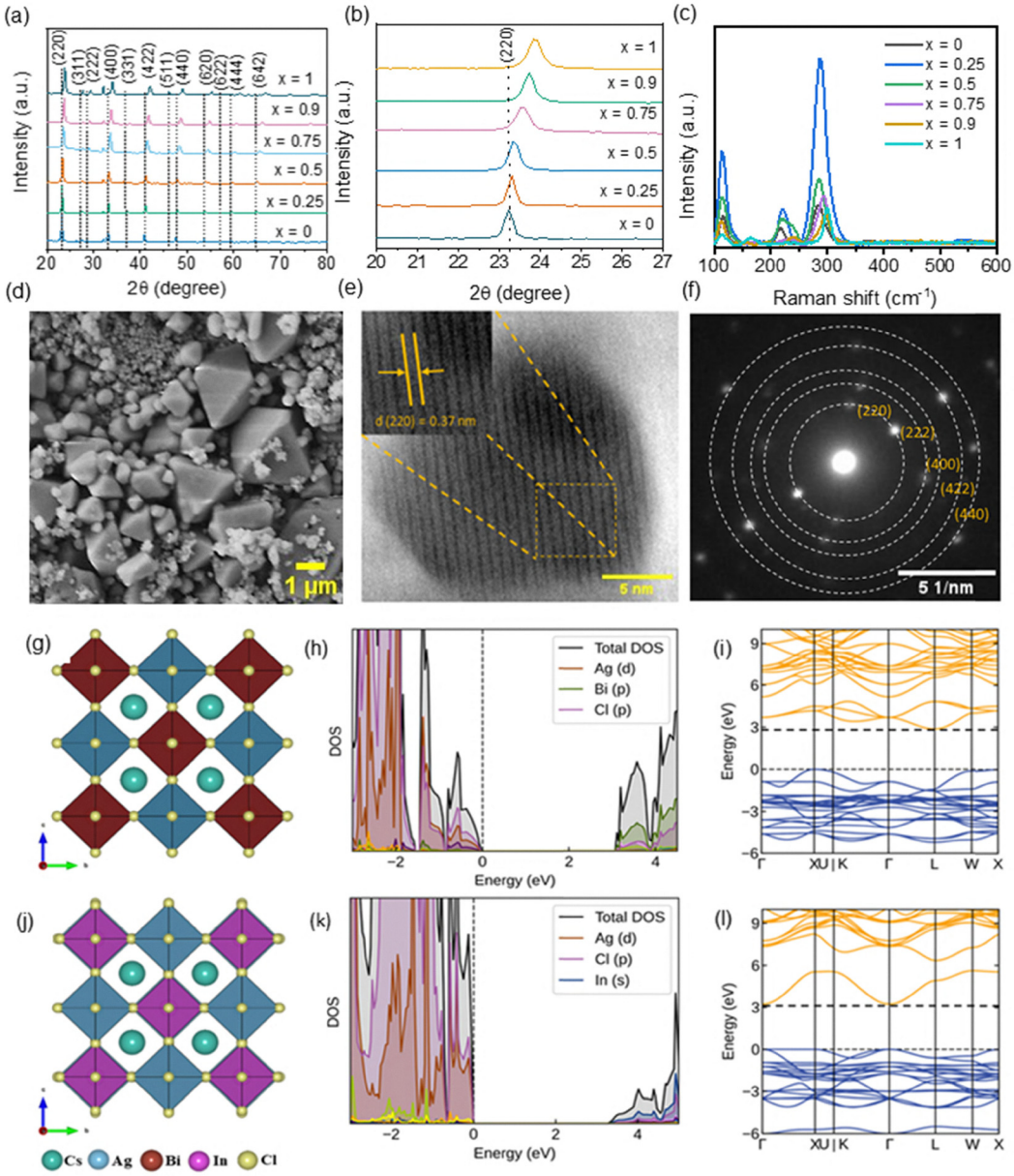

Fig. 1 (a) XRD pattern of $Cs_2AgIn_xBi_{1-x}Cl_6$ and (b) magnified XRD pattern showing a clear shift towards higher angles. (c) Raman spectra of $Cs_2AgIn_xBi_{1-x}Cl_6$. (d) FE-SEM image of the $Cs_2AgIn_xBi_{1-x}Cl_6$ (x = 0) sample. (e) and (f) High-resolution TEM image and SAED pattern of the $Cs_2AgIn_xBi_{1-x}Cl_6$ (x = 1) sample. (g) Crystal structure of $Cs_2AgIn_xBi_{1-x}Cl_6$ (x = 0). (h) The corresponding PDOS for $Cs_2AgIn_xBi_{1-x}Cl_6$ (x = 0). (i) Band structure of $Cs_2AgIn_xBi_{1-x}Cl_6$ (x = 0) along the high-symmetry directions of the Brillouin zone. (j) Crystal structure of $Cs_2AgIn_xBi_{1-x}Cl_6$ (x = 1). (k) The corresponding PDOS for $Cs_2AgIn_xBi_{1-x}Cl_6$ (x = 1). (l) Band structure of $Cs_2AgIn_xBi_{1-x}Cl_6$ (x = 1) along the high-symmetry directions of the Brillouin zone.

presents the Williamson–Hall (W–H) plots for $Cs_2AgIn_xBi_{1-x}Cl_6$ DPs. The average crystallite size (D), dislocation density (δ), and micro-strain (ε) estimated from W–H and Scherrer analyses for all the samples are summarized in the SI (Table S1). The

Table 1 Calculated structural parameters for the (220) plane from XRD

Material	Angle of diffraction, 2θ (degree)	D (nm)	δ ($\times 10^{14}$) lines per m^2	ε ($\times 10^{-3}$)	d (Å)	a (Å)
$Cs_2AgBiCl_6$	23.22	37.88	6.97	4.54	3.83	10.84
$Cs_2AgIn_{0.25}Bi_{0.75}Cl_6$	23.3	30.44	10.79	5.63	3.81	10.787
$Cs_2AgIn_{0.5}Bi_{0.5}Cl_6$	23.35	23.66	17.85	7.23	3.80	10.759
$Cs_2AgIn_{0.75}Bi_{0.25}Cl_6$	23.57	32.11	9.70	5.28	3.77	10.666
$Cs_2AgIn_{0.9}Bi_{0.1}Cl_6$	23.72	28.43	12.37	5.93	3.75	10.598
$Cs_2AgInCl_6$	23.87	23.23	18.54	21	3.72	10.530

 This journal is © the Owner Societies 2025

Open Access Article. Published on 04 September 2025. Downloaded on 1/29/2026 4:49:33 AM. This article is licensed under a Creative Commons Attribution 3.0 Unported Licence.

structural parameters for the (220) plane are also calculated and summarized in Table 1.

3.1.2 Raman Spectroscopy analysis. The Raman spectra of $Cs_2AgIn_xBi_{1-x}Cl_6$ DPs are shown in Fig. 1(c). A 532 nm wavelength laser was used to obtain the spectra. From the series of $Cs_2AgIn_xBi_{(1-x)}Cl_6$ DPs, $Cs_2AgIn_xBi_{(1-x)}Cl_6$ ($x = 0$) DPs consist of Cs^+ ions positioned at the core of the cuboctahedron having alternate [$BiCl_6$] and [$AgCl_6$] octahedral units, resulting in the creation of a three-dimensional grid,[51] whereas the DP structure of $Cs_2AgIn_xBi_{(1-x)}Cl_6$ ($x = 1$) is obtained by alternating [$AgCl_6$] and [$InCl_6$] octahedra in all three directions forming a 3D framework.[52] The $Cs_2AgIn_xBi_{1-x}Cl_6$ DPs exhibit three vibrational modes. The band at approximately 114 cm^{-1} corresponds to the breathing vibration of Ag–Cl bonds with T_{2g} symmetry. Additionally, the peaks observed at approximately 220 cm^{-1} and 285 cm^{-1} correspond to the stretching vibrations of the $AgCl_6$ octahedron having E_g and A_{1g} symmetry, respectively. Upon increasing In content from 10 to 90%, we observed a shift in the peaks along with changes in the intensities of each peak. Group theory predicts three types of Raman modes for $Cs_2AgIn_xBi_{1-x}Cl_6$ ($x = 1$): A_{1g}, E_g, and T_{2g}.[53] The peaks corresponding to these three modes occur at 113 (T_{2g}), 144 (E_g), and 300 (A_{1g}) cm^{-1}, respectively. The E_g and A_{1g} modes are assigned to the stretching vibrations of $AgCl_6$ and $InCl_6$ octahedra, respectively. There are two peaks corresponding to the T_{2g} mode with different frequencies, where the peak at a higher frequency is ascribed to the breathing of octahedra and the peak at a lower frequency is due to the translational motion of the Cs^+ ion.[54] The slight shift in Raman peaks suggests that incorporating In into the host material has induced lattice strain, indicating an improvement in the crystallinity of the samples.

3.1.3 FE-SEM/EDS analysis. Fig. 1(d) shows the field emission-scanning electron microscopy (FE-SEM) image of $Cs_2AgIn_xBi_{1-x}Cl_6$ ($x = 0$) DPs captured at a 1 μm scale. The image shows the formation of cubic crystals. The FE-SEM images of $Cs_2AgIn_xBi_{1-x}Cl_6$ ($x = 0.50$, 0.75, 0.90, and 1.0) captured at a 200 nm scale are provided in Fig. S4 of the SI. From the FE-SEM images, it can be observed that the cubic crystal structure is maintained after In alloying. Compositional analysis of the $Cs_2AgIn_xBi_{1-x}Cl_6$ DPs was conducted using EDS. The EDS spectra of all samples are shown in Fig. S5 of the SI. Elemental analysis using the EDS technique was employed to determine the actual concentration of indium in the $Cs_2AgIn_xBi_{1-x}Cl_6$ NCs. The atomic percentages are listed in Table S3 of the SI. EDS spectra were acquired in the binding energy range of 0–15 keV for the $Cs_2AgIn_xBi_{1-x}Cl_6$ DPs, revealing a nearly stoichiometric composition of the synthesized material. Moreover, the obtained atomic composition closely corresponds to that of the metal salts used. The atomic composition analysis reveals a continuous decrease in the Bi content and an increase in the In content, with the latter increasing during the synthesis. The elemental mapping images of $Cs_2AgIn_xBi_{1-x}Cl_6$ ($x = 0$, 0.50, 0.75, 0.9, 1.0) samples are shown in Fig. S6–S10, respectively, of the SI. EDS mapping images confirm the homogeneous dispersion of all elements within the synthesized materials.

3.1.4 Transmission Electron Microscopy (TEM) analysis. The low-resolution TEM images of $Cs_2AgIn_xBi_{1-x}Cl_6$ ($x = 0$, 1) and the corresponding histograms are shown in Fig. S2 of the supporting information. The average particle size estimated for $Cs_2AgIn_xBi_{1-x}Cl_6$ ($x = 0$) DPs is around 24.7 nm, and it is 17.7 nm for $Cs_2AgIn_xBi_{1-x}Cl_6$ ($x = 1$). Fig. 1(e) shows the HR-TEM image of $Cs_2AgIn_xBi_{1-x}Cl_6$ ($x = 1$) NCs recorded at a resolution of 5 nm. The TEM image shows the cubic morphology of the $Cs_2AgIn_xBi_{1-x}Cl_6$ ($x = 1$) DPs. As observed, the high-resolution TEM image (Fig. 1(e)) reveals clear lattice fringes. For $Cs_2AgIn_xBi_{1-x}Cl_6$ ($x = 1$), the value of interplanar spacing is approximately 0.37 nm as derived from the TEM images, which represents the orientation along (220) planes. The selected-area electron diffraction (SAED) pattern of $Cs_2AgIn_xBi_{1-x}Cl_6$ ($x = 1$) shows concentric rings corresponding to the (220), (222), (400), (422), and (440) lattice planes as shown in Fig. 1(f). These results are consistent with those obtained from XRD. The presence of prominent diffraction spots in the SAED pattern confirms the polycrystalline nature of the materials. Additional HR-TEM images at a resolution of 5 nm and the corresponding SAED patterns, along with the respective lattice planes, for $Cs_2AgIn_xBi_{1-x}Cl_6$ DPs are provided in the SI (Fig. S3).

Furthermore, we performed first-principles DFT calculations to characterize the structural and electronic structures of $Cs_2AgIn_xBi_{1-x}Cl_6$ ($x = 0$, 1). Both materials were modeled in the cubic $Fm\bar{3}m$ space group as displayed in Fig. 1(g) and (j). The optimized lattice parameter is calculated to be $a = 10.88$ Å (1287.19 $Å^3$) for $Cs_2AgIn_xBi_{1-x}Cl_6$ ($x = 0$) and 10.61 Å (1194.59 $Å^3$) for $Cs_2AgIn_xBi_{1-x}Cl_6$ ($x = 1$), aligning well with the experimental findings. The observed contraction in the lattice parameter of $Cs_2AgIn_xBi_{1-x}Cl_6$ ($x = 1$) compared to $Cs_2AgIn_xBi_{1-x}Cl_6$ ($x = 0$) is consistent with the larger ionic size of Bi^{3+} (117 pm) than In^{3+} (94 pm). The partial density of states (PDOS) analysis demonstrated that the valence band (VB) edge of the $Cs_2AgIn_xBi_{1-x}Cl_6$ ($x = 0$) NCs (Fig. 1(h)) is dominated by Cl-p and Ag-d orbitals, whereas the Bi-p orbitals dominate the conduction band (CB) edge.

Similarly, for the $Cs_2AgIn_xBi_{1-x}Cl_6$ ($x = 1$) NCs (Fig. 1(k)), the VB edge is dominated by Cl-p and Ag-d orbitals, whereas In-s dominates the CB edge. It is evident from the predicted electronic band structures displayed in Fig. 1(i) and (l) that the $Cs_2AgIn_xBi_{1-x}Cl_6$ ($x = 0$) NCs exhibit an indirect band gap of 2.87 eV, whereas the $Cs_2AgIn_xBi_{1-x}Cl_6$ ($x = 1$) NCs exhibit a direct band gap of 3.24 eV at the Γ-point on the Brillouin zone. These results confirmed the transition from indirect to direct with the complete replacement of Bi^{3+} with In^{3+} ions.

The effective mass values of electrons (m_e^*) and holes (m_h^*) along the directions of different Brillouin zones in the $Cs_2AgIn_xBi_{1-x}Cl_6$ ($x = 0.0$, 1.0) NCs are determined using the equation:

$$m^*_{e(h)} = \pm\hbar^2\left(\frac{d^2E_k}{dk^2}\right)^{-1},$$

where E_k is the energy of the band (*i.e.*, CBM and VBM) as a function of the wave vector k, and $\hbar$ is the reduced Planck's

Open Access Article. Published on 04 September 2025. Downloaded on 1/29/2026 4:49:33 AM. This article is licensed under a Creative Commons Attribution 3.0 Unported Licence.

constant. For $Cs_2AgIn_xBi_{1-x}Cl_6$ (x = 0), the $m_e^*(m_h^*)$ values are calculated to be 0.490 ($-0.233m_e$) and 0.351 ($-1.004m_e$) along the X–Γ and X–W directions, respectively. For $Cs_2AgIn_xBi_{1-x}Cl_6$ (x = 1.0), the $m_e^*(m_h^*)$ values are predicted to be 0.309 ($-0.322m_e$), 0.316 ($-0.450m_e$), and 0.319 ($-0.666m_e$) along the Γ–X, Γ–K, and Γ–L directions, respectively. Generally, the predicted electron effective masses are smaller as compared to the hole effective masses, except for the X–Γ direction for $Cs_2AgBiCl_6$, suggesting a higher electron mobility compared to hole mobility in these materials. The larger electron effective mass along the X–Γ direction for $Cs_2AgBiCl_6$ than the hole effective mass can be attributed to the small curvature (less dispersed bands) at the conduction band edge along the X–Γ direction compared to that of the valence band edge. The Bohr exciton radius is estimated for $Cs_2AgIn_xBi_{1-x}Cl_6$ (x = 0, 1) by using the results obtained from first principles DFT calculations. A detailed explanation can be found in the SI. The estimated Bohr radius is 1.3 nm for $Cs_2AgIn_xBi_{(1-x)}Cl_6$ (x = 0) and 0.82 nm for $Cs_2AgIn_xBi_{(1-x)}Cl_6$ (x = 1). These values are much smaller than the size of the crystals determined from the TEM histogram, strongly suggesting a weak quantum confinement in both materials.

3.1.5 X-ray Photoelectron Spectroscopy (XPS) analysis. Fig. 2 shows the XPS spectra of $Cs_2AgIn_xBi_{1-x}Cl_6$ NCs, revealing the presence of Cs, Ag, In, Bi, and Cl in the prepared NCs. To further comprehend the effect of incorporating In on the electronic properties, core level XPS spectra were recorded for Cs 3d, In 3d, Ag 3d, Cl 2p, and Bi 4f, and are displayed in Fig. 2. The binding energy values for electrons were calculated, with correction for the shift in carbon 1s binding energy. For $Cs_2AgIn_xBi_{1-x}Cl_6$ (x = 0), Cs-$3d_{3/2}$ and Cs-$3d_{5/2}$ peaks are observed at 740.70 eV and 726.76 eV, as shown in Fig. 2(a1).

In the narrow Ag 3d XPS spectrum, peaks around 376 eV and 370 eV (Fig. 2(a2)) correspond to Ag-$3d_{3/2}$ and Ag-$3d_{5/2}$. The Bi-4f spectrum exhibits a doublet at 161.43 eV and 166.80 eV, indicating the presence of bismuth in a 3+ state. Cl 2p spectra display peaks at approximately 202 eV and 204 eV for Cl $2p_{3/2}$ and Cl $2p_{1/2}$. For the $Cs_2AgIn_xBi_{1-x}Cl_6$ (x = 0.5) sample, the two peaks are detected in the elemental scan of Cs 3d located at 723.70 eV and 737.66 eV.

These peaks are associated with the Cs $3d_{5/2}$ and Cs $3d_{3/2}$ states. The narrow scan XPS of Ag reveals peaks at around 367 eV and 373 eV for $3d_{5/2}$ and $3d_{3/2}$, respectively. The two peaks at 158.55 eV and 164 eV in the narrow scan XPS spectrum of Bi 4f signify Bi $4f_{7/2}$ and $4f_{5/2}$ states. The narrow scan spectrum of In 3d exhibits peaks at 444.73 eV and 452.14 eV. Cl 2p narrow scan deconvolution reveals peaks at 197.11 eV and 198.44 eV for $2p_{3/2}$ and $2p_{1/2}$ (Fig. 2(b1)–(b5)). For $Cs_2AgIn_xBi_{1-x}Cl_6$ (x = 0.75) (Fig. 2(c1)–(c5)), narrow scan XPS of Cs 3d shows peaks at 738 eV ($3d_{3/2}$) and 724 eV ($3d_{5/2}$).

The Ag elemental scan reveals peaks around 367.8 eV and 373.8 eV for Ag $3d_{5/2}$ and Ag $3d_{3/2}$, respectively. The Bi 4f narrow scan displays a doublet at 158.88 and 164.42 eV for Bi $4f_{7/2}$ and $4f_{5/2}$, respectively. The In 3d narrow scan exhibits peaks at 445.18 eV and 452.6 eV for In $3d_{5/2}$ and $3d_{3/2}$ states, respectively. Cl 2p narrow scan deconvolution reveals peaks at 198.19 eV and 199.98 eV for $2p_{3/2}$ and $2p_{1/2}$. No additional peak was observed in any of the narrow scans, indicating that no metallic phase present for any of the elements. The narrow scan XPS spectrum of cesium in $Cs_2AgIn_xBi_{1-x}Cl_6$ (x = 1) shows two spin–orbit states at 723.58 eV and 737.45 eV for $3d_{5/2}$ and $3d_{3/2}$, respectively (Fig. S12(b2)–(b5), SI).[31] The peaks observed at 367.22 eV and 373.25 eV are attributed to the Ag $3d_{5/2}$ and $3d_{3/2}$ levels, respectively, which confirms that Ag is present in the +1 oxidation state. In the narrow scan XPS spectrum, two peaks corresponding to the In $3d_{5/2}$ and $3d_{3/2}$ states are observed at 444.44 eV and 452 eV, respectively.[55] The deconvolution of the narrow scan XPS spectrum of chlorine shows $2p_{3/2}$ and $2p_{1/2}$ fine levels at 197.66 and 199.29 eV, respectively. The XPS spectra of $Cs_2AgIn_xBi_{1-x}Cl_6$ (x = 0.1, 0.25, 0.90, 1.0) are provided in Fig. S11 and S12 of the SI.

3.2 Optical properties of $Cs_2AgIn_xBi_{(1-x)}Cl_6$ DPs

3.2.1 UV-visible spectroscopy. Fig. 3(a) displays the optical absorption spectra of $Cs_2AgIn_xBi_{(1-x)}Cl_6$ derived from diffuse reflectance spectra. An excitonic peak at 365 nm and a tail extending towards higher wavelengths is observed in the UV-vis spectrum of $Cs_2AgBiCl_6$ (x = 0). This peak originates from the bismuth $6s^2$–$6s^1$ $6p^1$ direct transition, whereas the long tail arises due to the transitions related to the trap state along with the indirect band gap.[25,28,30] An indirect band gap transition is an inherent property of a material that results in a low photoluminescence quantum efficiency (PLQE). These findings suggest that the $Cs_2AgIn_xBi_{1-x}Cl_6$ (x = 0) NCs are not appropriate for application in the field of optoelectronics.[56] As the In content is increased, the absorption peak shows a blue shift, and the absorption tail is reduced. The absorption edge is relatively sharp for the In contents of 75% and 90%, highlighting the direct band gap of $Cs_2AgIn_xBi_{(1-x)}Cl_6$ (x = 0.75 and 0.9). The absorption peak is located at ∼280 nm in the case of $Cs_2AgIn_xBi_{1-x}Cl_6$ (x = 1), with a band gap value of 3.5 eV. This DP exhibits poor absorption near the band gap; therefore, it is not a suitable choice for optoelectronic applications.[57] The values of the band gap were estimated by using the following equation:

$$[F(R_\infty)h\nu]^n = A(h\nu - E_g) \quad (5)$$

where $h\nu$ represents the incident energy, A is the proportionality constant, E_g represents the optical band gap, n is an integer, and its values are 2 and $\frac{1}{2}$ for the allowed direct and indirect transitions, respectively, and $F(R_\infty)$ is the Kubelka–Munk function, which is expressed as

$$F(R_\infty) = \frac{(1-R)^2}{2R} = \frac{K}{S} \quad (6)$$

where R, K, and S are the reflection, absorption, and scattering coefficients, respectively.

For $Cs_2AgIn_xBi_{1-x}Cl_6$ (x = 0, 0.25, 0.5) samples, the band gap was determined by extrapolation of the linear portion of $[F(R_\infty)(h\nu)]^{1/2}$ *versus* $h\nu$ in the Tauc plot (Fig. S13). The band gap value increases from 2.71 eV for the pristine sample (x = 0) to 2.81 eV for the $Cs_2AgIn_xBi_{1-x}Cl_6$ (x = 0.5) sample. The band

 This journal is © the Owner Societies 2025

Open Access Article. Published on 04 September 2025. Downloaded on 1/29/2026 4:49:33 AM.
This article is licensed under a Creative Commons Attribution 3.0 Unported Licence.

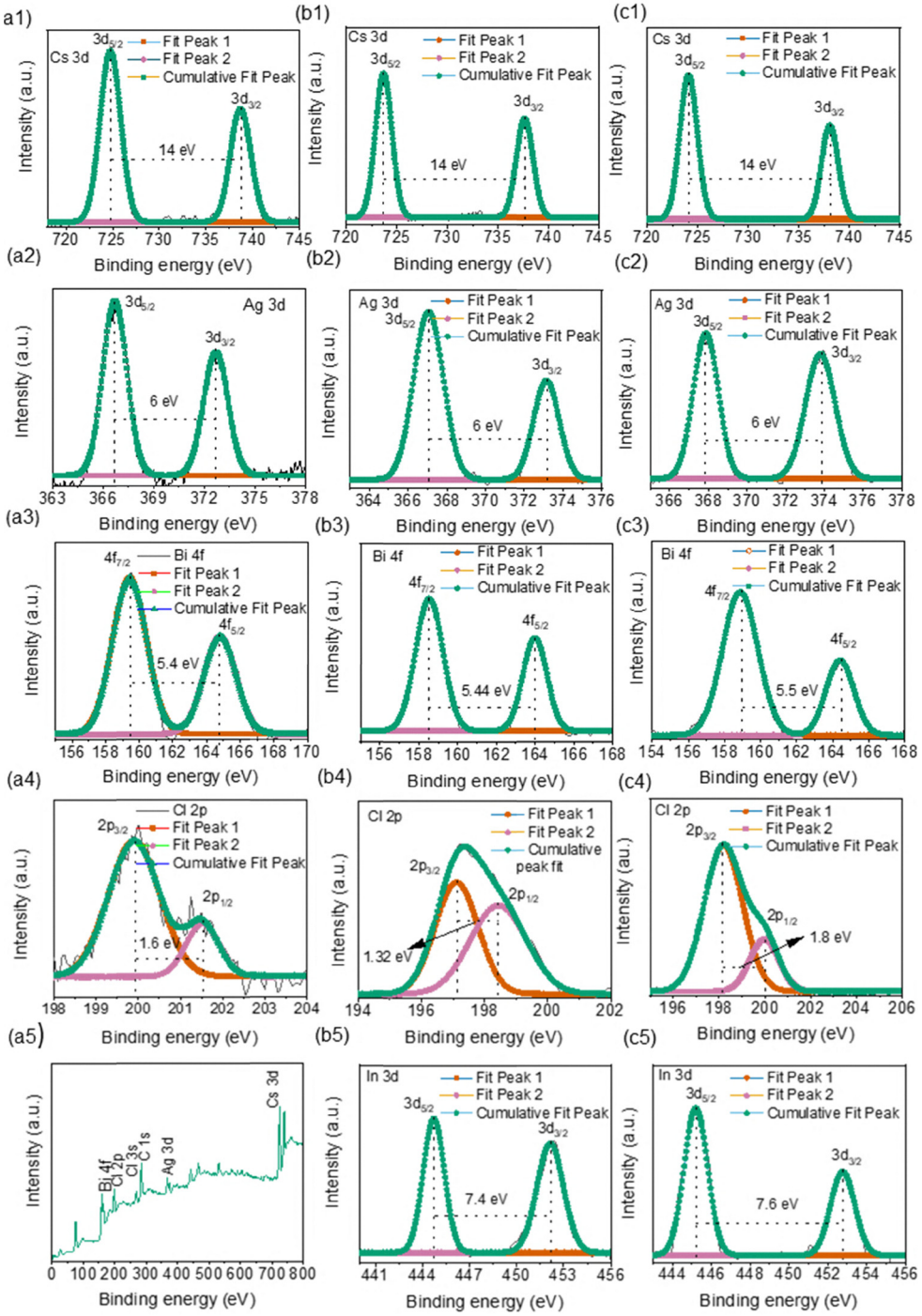

Fig. 2 (a1)–(a5) Narrow scan and survey scan XPS spectra of the $Cs_2AgIn_xBi_{1-x}Cl_6$ (x = 0) sample. (b1)–(b5) Narrow scan XPS spectra of the $Cs_2AgIn_xBi_{1-x}Cl_6$ (x = 0.5) sample. (c1)–(c5) Narrow scan XPS spectra of the $Cs_2AgIn_xBi_{1-x}Cl_6$ (x = 0.75) sample.

gap variation can be attributed to changes in the electronic structure of the material. On the other hand, as it is well reported that above 50%. In content, the band gap nature changes from indirect to direct, the band gap values for the samples with In content more than 50% are determined by extrapolation of the linear region in the $[F(R_\infty)h\nu]^2$ *versus* $h\nu$ plot (Fig. S12).[33] The estimated optical band gap values are provided in Table S2 of the SI. The optical properties of $Cs_2AgIn_xBi_{1-x}Cl_6$ (x = 0, 1) DPs (Fig. 3(b)–(e)) show that they exhibit weak optical absorption around the band gap. $Cs_2AgIn_xBi_{1-x}Cl_6$ (x = 0) has a higher dielectric constant (3.89) than $Cs_2AgIn_xBi_{1-x}Cl_6$ (x = 1) (2.89), indicating its higher ability to screen charge carriers and reduce recombination rates. The $Cs_2AgIn_xBi_{1-x}Cl_6$ (x = 0) material also possesses higher reflectivity and refractive index than $Cs_2AgIn_xBi_{1-x}Cl_6$ (x = 1), as shown in Fig. 3(d) and (e).

Open Access Article. Published on 04 September 2025. Downloaded on 1/29/2026 4:49:33 AM.
This article is licensed under a Creative Commons Attribution 3.0 Unported Licence.

3.2.2 Photoluminescence (PL) studies. The In-alloyed DP NCs were further characterized through room-temperature photoluminescence (PL). Fig. 3(f) shows the Jacobian-transformed PL spectra of $Cs_2AgIn_xBi_{(1-x)}Cl_6$ NCs. All samples were excited using a wavelength of 365 nm. The room temperature PL of $Cs_2AgIn_xBi_{1-x}Cl_6$ (x = 0) exhibits broadband emission, featuring an excitonic peak around 575 nm alongside emissions related to defects. For $Cs_2AgIn_xBi_{1-x}Cl_6$ (x = 0.0, 0.25, and 0.50), the PL profiles closely resemble that of the $Cs_2AgIn_xBi_{1-x}Cl_6$ (x = 0) sample, differing primarily in the intensity. Nonetheless, peak positions exhibit slight shifts, suggesting tunability in the emission wavelengths of the NCs consistent with the absorption spectroscopy results. As the In content increases above 50%, dual emissions emerge in the PL spectra, observed in the blue-violet and orange regions. Among them, the narrow peak located at high-energy in the PL of $Cs_2AgIn_xBi_{1-x}Cl_6$ (x = 0.75, 0.90) likely originates from the free exciton emission, whereas the broad low-energy peak is ascribed to the emissions arising from defects or self-trapped excitons (STEs). In contrast to free excitons, defects and STEs' emission spectra are broad with a large Stoke's shift from the absorption. Initially, the PL peak gradually rises, but beyond x = 0.75, the intensity experiences a sudden increase. The photoluminescence excitation spectra for all the samples were recorded and are shown in Fig. S18 of the SI. Fig. S18(a)–(c) show that the PLE spectrum has its onset wavelength lower than the absorption onset, further confirming the indirect band gap nature of $Cs_2AgIn_xBi_{1-x}Cl_6$ (x = 0, 0.25, 0.5). Fig. S18(d)–(g) presents the PLE spectra recorded for Cs_2AgIn_x-$Bi_{1-x}Cl_6$ (x = 0.75, 0.90) samples corresponding to emissions in the violet/blue as well as the yellow/orange region. The excitation spectra of $Cs_2AgIn_xBi_{1-x}Cl_6$ (x = 0.75, 0.90) samples corresponding to emissions in the blue-violet region ideally overlap with the absorption spectra of these samples, which confirms that the materials can be classified as direct band gap materials. Furthermore, it is confirmed that the broad orange/yellow emissions in the case of $Cs_2AgIn_xBi_{1-x}Cl_6$ (x = 0.75, 0.90) samples are attributed to the excited-state defects, indicating

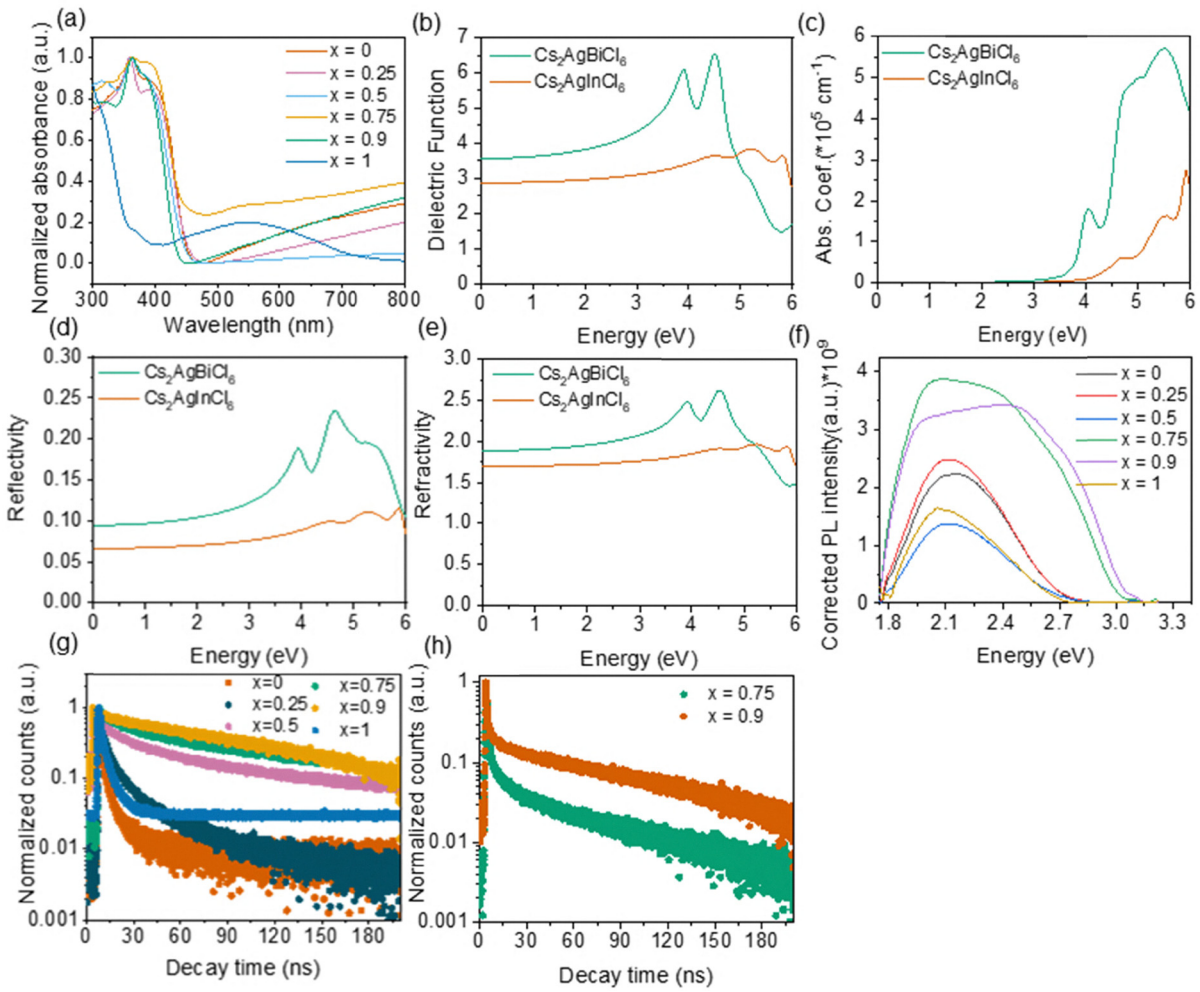

Fig. 3 (a) Optical absorption spectra of $Cs_2AgIn_xBi_{(1-x)}Cl_6$ derived from diffuse reflectance spectra. (b)–(e) DFT calculated optical properties of $Cs_2AgIn_xBi_{1-x}Cl_6$ (x = 0) and $Cs_2AgIn_xBi_{1-x}Cl_6$ (x = 1): (b) dielectric function, (c) absorption coefficient, (d) reflectivity, and (e) refractive index. (f) Jacobian transformed room temperature PL spectra of $Cs_2AgIn_xBi_{(1-x)}Cl_6$. (g) and (h) TRPL traces of $Cs_2AgIn_xBi_{(1-x)}Cl_6$ corresponding to emissions towards higher and lower wavelengths, respectively.

 This journal is © the Owner Societies 2025

Open Access Article. Published on 04 September 2025. Downloaded on 1/29/2026 4:49:33 AM. This article is licensed under a Creative Commons Attribution 3.0 Unported Licence.

that there is a slight change in the crystal structure of the material.

3.2.3 Time-resolved Photoluminescence (TRPL) analysis. To confirm the origin of dual emission in the synthesized $Cs_2AgIn_xBi_{(1-x)}Cl_6$ DP NCs, TRPL measurements were carried out. A picosecond 405 nm laser diode was used as an excitation source, which could generate a pulse width shorter than 70 ps. The decay curves for all the samples were recorded corresponding to the broad emission, and the decay traces are shown in Fig. 3(g). The decay traces for $Cs_2AgIn_xBi_{1-x}Cl_6$ (x = 0.75, 0.9) samples, which correspond to the violet/blue emissions, are shown in Fig. 3(h). The emission decay traces are fitted with a function:

$$A(t) = A_1 \exp\left(\frac{-t}{\tau_1}\right) + A_2 \exp\left(\frac{-t}{\tau_2}\right) \quad (7)$$

where τ_1 and τ_2 are the decay components. The first short lifetime PL component in bi-exponential decay arises from excitonic recombination, while the second long lifetime PL component is due to the trap state-related excitonic recombination. The average lifetime (t) is calculated using the formula:

$$t_{av} = \frac{A_1\tau_1^2 + A_2\tau_2^2}{A_1\tau_1 + A_2\tau_2} \quad (8)$$

For $Cs_2AgIn_xBi_{1-x}Cl_6$ (x = 0.75 or x = 0.9) samples, the decay traces corresponding to violet/blue emission show quick decay, while the decay corresponding to orange/yellow PL is much slower (Table S4). The distinctly different decay profiles of the two emissions indicate that their origins are different. For $Cs_2AgIn_xBi_{1-x}Cl_6$ (x = 0.75, 0.9) samples, the TRPL corresponding to a high energy peak shows a fast decay of less than 2 ns. The lifetime values calculated for broad orange/yellow emissions are approximately 141 ns and 167 ns, respectively, for $Cs_2AgIn_xBi_{1-x}Cl_6$ (x = 0.75, 0.9) samples. The TRPL calculations showed a sudden increase in the lifetime of charge carriers upon increasing the concentration of In up to 90%, and it again decreased suddenly at x = 1, indicating the excellent optical properties of $Cs_2AgIn_xBi_{1-x}Cl_6$ (x = 0.75, 0.9). The lifetime values calculated from TRPL measurements and the contributions from short and long decay components are listed in Table 2.

3.3 Electrochemical measurements

Fig. 4(a) shows the cyclic voltammogram of $Cs_2AgIn_xBi_{(1-x)}Cl_6$ (x = 0) DPs recorded at a 50 mV scan rate. The CV measurements were performed to examine the electronic band structure of the synthesized $Cs_2AgIn_xBi_{(1-x)}Cl_6$ DP materials. The blank CV was recorded in the DCM–TBAP mixture to verify the absence of any redox processes. The working electrode was fabricated by drop-casting 50 μL (at a concentration of 1 mg mL^{-1}) of the perovskite sample and subsequently drying under vacuum. The cyclic voltammograms of the $Cs_2AgIn_xBi_{(1-x)}Cl_6$ (x = 0.25, 0.5, 0.75, 1) DPs are shown in Fig. 4(b)–(e), respectively. The CV recorded for the $Cs_2AgIn_xBi_{(1-x)}Cl_6$ (x = 0) sample shows two distinct peaks corresponding to the oxidation and reduction taking place at the respective electrodes. The peak at 1.98 V is the anodic (oxidation) peak that corresponds to the removal of an electron from the VB. On the other hand, the peak at −0.7 V is the cathodic (reduction) peak that corresponds to the addition of an electron to the CB. The CB and VB edge positions with respect to the vacuum level for the x = 0 sample are −3.8 and −6.48 eV, respectively. The electrochemical band gap (E_c) is determined as a potential difference between the anodic and cathodic peaks observed from the redox reactions taking place at the semiconductor–electrolyte interface, and it is measured at 2.68 eV for the $Cs_2AgIn_xBi_{1-x}Cl_6$ (x = 0) sample. This is consistent with the optical band gap value determined from UV-vis spectroscopy. The comparison of the optical and electrochemical band gap values is shown in Fig. S15 of the SI. The same procedure was followed to determine the band gap and positions of band edges for the other materials. The observed anodic and cathodic peak positions are shown in Table 3. The band edge positions for all the samples are determined with respect to the normal hydrogen electrode (NHE) and local vacuum and summarized in Table 3.[42,58] Scan rate-dependent CV measurements were performed for the $Cs_2AgIn_xBi_{1-x}Cl_6$ (x = 0.25) sample to investigate the scan rate dependence of current. The CV recorded with increasing scan rates is shown in Fig. 4(f) and (g). The linearly increasing current with the square root of the scan rate for cathodic and anodic peaks suggests that the reaction is diffusion-controlled.[39,58,59] Fig. 4(h) displays the band alignment diagram of $Cs_2AgIn_xBi_{(1-x)}Cl_6$ (x = 0.0, 0.25, 0.50, 0.75, 1.0). The figure shows the CBM and VBM positions determined for these materials *vs.* local vacuum, as well as the electrochemical band gaps estimated from the CV measurements.

3.4 Temperature-dependent Photoluminescence analysis

Fig. 5 displays the Jacobian transformed PL spectra of $Cs_2AgIn_xBi_{(1-x)}Cl_6$ (x = 0, 0.75, 0.9) recorded from 80 K to 300 K. Excitation of the samples was achieved using a wavelength of 365 nm. The PL exhibits broadband emission, attributed to self-trapped excitons (STEs). The broad PL emission is elucidated by the self-trapped states induced by exciton–phonon coupling. To assess the exciton–phonon coupling strength, TDPL measurements were carried out. For $Cs_2AgIn_xBi_{(1-x)}Cl_6$ (x = 0) DPs, when the temperature increases from 80 K to 300 K, the intensity of the peak is reduced along with the broadening of peaks. Additionally, the peak is blue-shifted up to 200 K, followed by a red shift with higher temperature. These shifts can be attributed to lattice distortion and changes in the valence band

Table 2 Calculated decay components (τ_1 and τ_2) and average carrier lifetimes (t) for $Cs_2AgIn_xBi_{(1-x)}Cl_6$

Material	τ_1 (ns)	% A_1	τ_2 (ns)	% A_2	t (ns)	R^2
$Cs_2AgBiCl_6$	1.09	99.92	5.92	0.08	1.11	0.997
$Cs_2AgIn_{0.25}Bi_{0.75}Cl_6$	2.67	97.09	17.60	2.91	5.13	0.996
$Cs_2AgIn_{0.5}Bi_{0.5}Cl_6$	5.45	67.54	48.07	32.46	39.94	0.997
$Cs_2AgIn_{0.75}Bi_{0.25}Cl_6$	15.35	59.51	158.79	40.49	140.95	0.96
$Cs_2AgIn_{0.9}Bi_{0.1}Cl_6$	9.85	25.98	170.16	74.02	166.97	0.992
$Cs_2AgInCl_6$	1.56	98.43	5.76	1.57	1.79	0.999

Open Access Article. Published on 04 September 2025. Downloaded on 1/29/2026 4:49:33 AM.
This article is licensed under a Creative Commons Attribution 3.0 Unported Licence.

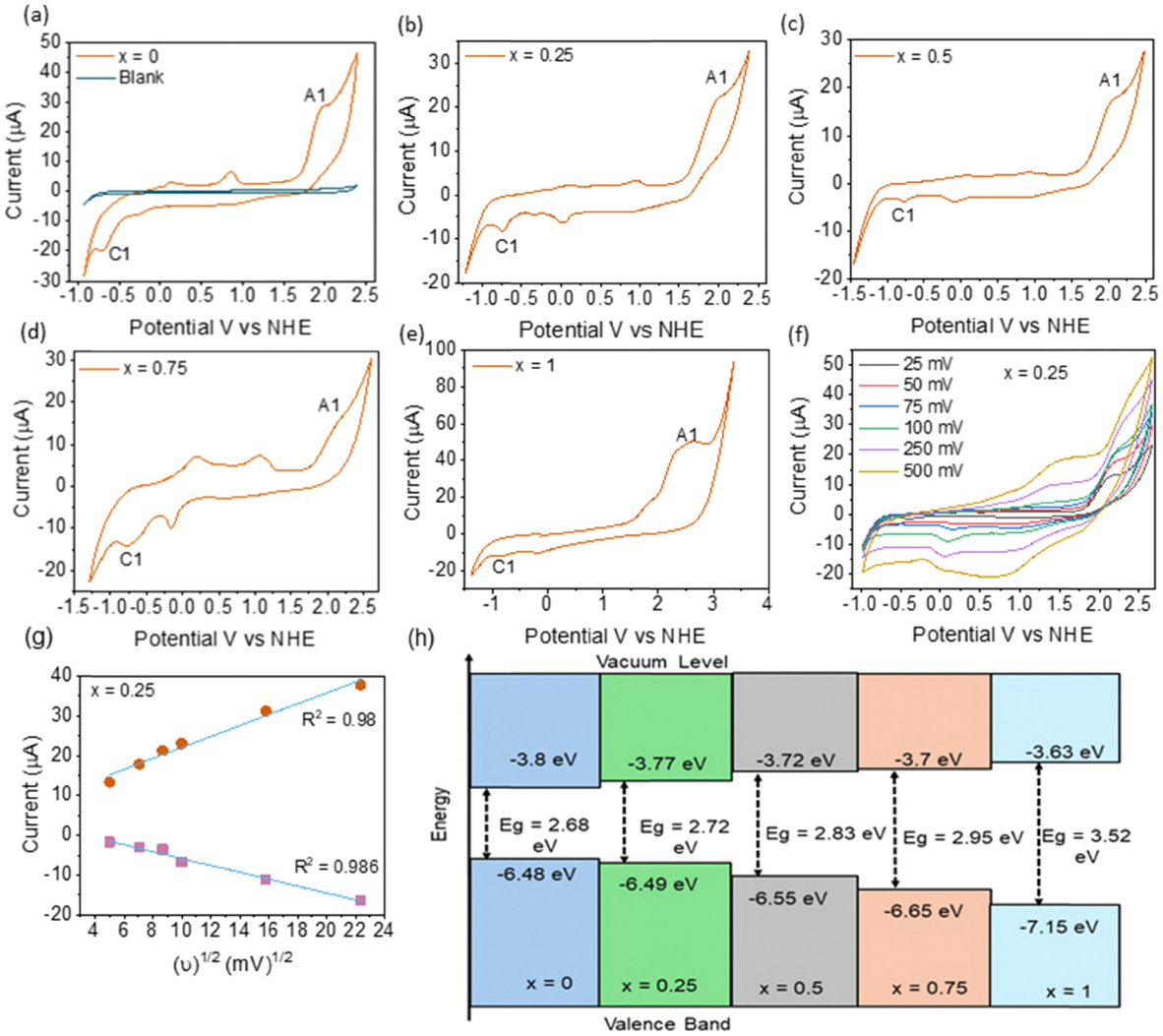

Fig. 4 (a) Cyclic voltammogram of the $Cs_2AgIn_xBi_{1-x}Cl_6$ (x = 0) sample compared with the blank CV. (b)–(e) Cyclic voltammograms of $Cs_2AgIn_xBi_{1-x}Cl_6$ (x = 0.25, 0.5, 0.75 and 1, respectively). (f) Scan rate dependent CV for the $Cs_2AgInxBi_{(1-x)}Cl_6$ (x = 0.25) sample. (g) Linear fitting of the scan rate dependent CV data as a square root of the scan rate *vs.* current using the Randles–Sevcik equation for the $Cs_2AgIn_xBi_{(1-x)}Cl_6$ (x = 0.25) sample. (h) Band alignment diagram.

Table 3 The VB and CB edge positions *vs.* NHE and vacuum, and electrochemical band gaps evaluated using CV measurements

Sample	CBM *vs.* NHE (V)	VBM *vs.* NHE (V)	CBM *vs.* vacuum (eV)	VBM *vs.* vacuum (eV)	E_c (eV)	E_g (eV)
$Cs_2AgBiCl_6$	−0.7	1.98	−3.8	−6.48	2.68	2.70
$Cs_2AgIn_{0.25}Bi_{0.75}Cl_6$	−0.73	1.99	−3.77	−6.49	2.72	2.71
$Cs_2AgIn_{0.5}Bi_{0.5}Cl_6$	−0.78	2.05	−3.72	−6.55	2.83	2.81
$Cs_2AgIn_{0.75}Bi_{0.25}Cl_6$	−0.8	2.15	−3.7	−6.65	2.95	2.89
$Cs_2AgInCl_6$	−0.87	2.65	−3.63	−7.15	3.52	3.53

concerning temperature variations. The Jacobian transformed TDPL spectra of $Cs_2AgIn_xBi_{(1-x)}Cl_6$ (x = 0.25, 0.5, 1) are shown in Fig. S16 of the SI. The intensity of PL peaks first increases up to 160 K and then decreases at higher temperatures in the case of $Cs_2AgIn_xBi_{(1-x)}Cl_6$ (x = 0.25 and 0.5) samples. The FWHM broadens with an increase in temperature. Also, there is a blue shift in PL peak positions. In the case of the $Cs_2AgIn_xBi_{(1-x)}Cl_6$ (x = 1) sample, the intensity decreases monotonically along with a blue shift in PL peaks. For $Cs_2AgIn_xBi_{(1-x)}Cl_6$ (x = 0.75, 0.90) samples, the emission originating from STEs became dominant over the free exciton emission with decreasing temperature from 300 K to 80 K, as shown in Fig. 5(b) and (c). The peak position of STE PL exhibited a slight red shift, while that of the free exciton PL was unchanged when the temperature decreased. As can be seen clearly, the STEs' peak profile became comparatively narrower with a decrease in temperature. Non-radiative recombination is hindered at low temperatures, and hence we obtain maximum intensity at lower temperatures.

The corrected PL intensity *vs.* inverse temperature (Fig. 5) is fitted with $R^2 \approx 1$ using an Arrhenius equation:

$$I(T) = \frac{I_0}{1 + A\exp\left(\frac{-E_a}{k_B T}\right)} \quad (9)$$

where $I(T)$ and I_0 are the corrected PL intensity values at

 This journal is © the Owner Societies 2025

Open Access Article. Published on 04 September 2025. Downloaded on 1/29/2026 4:49:33 AM.
This article is licensed under a Creative Commons Attribution 3.0 Unported Licence.

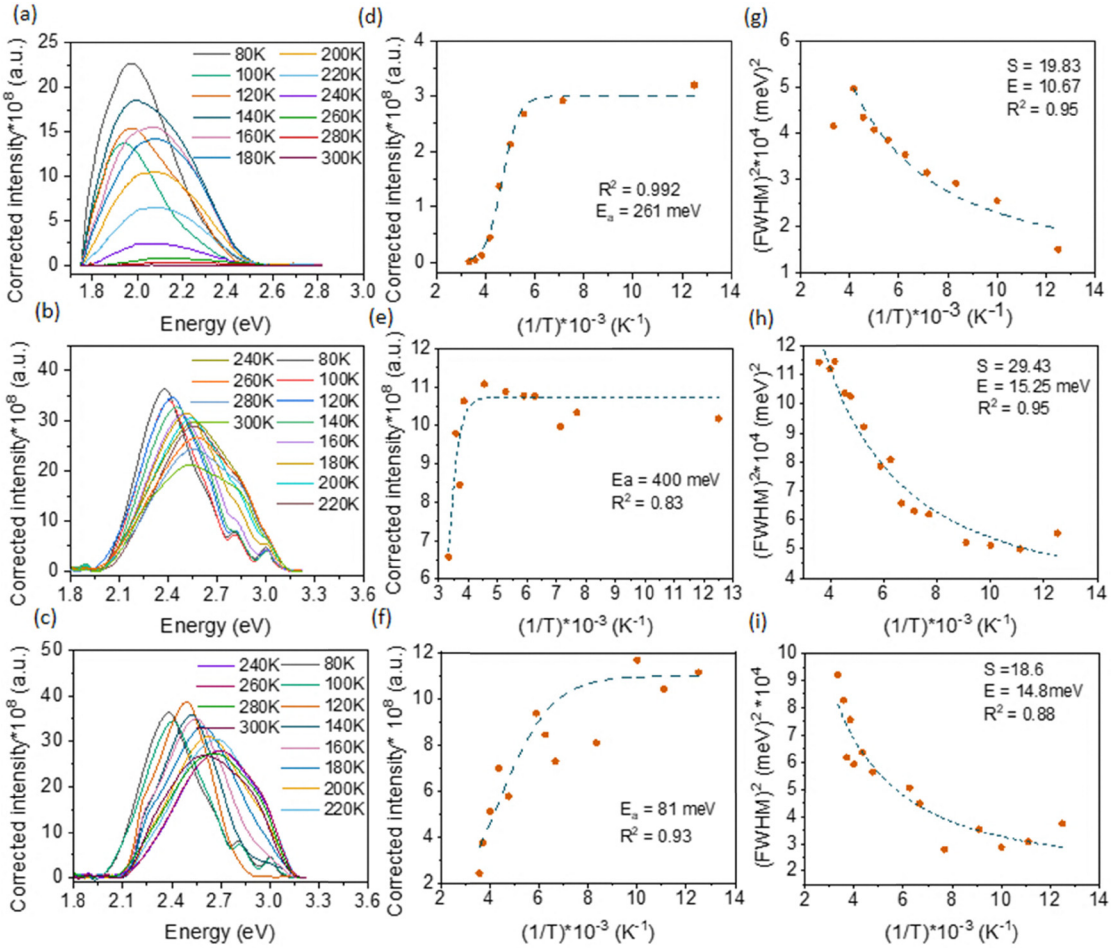

Fig. 5 (a)–(c) The Jacobian transformed TDPL spectra of $Cs_2AgIn_xBi_{(1-x)}Cl_6$ recorded in the temperature range 80–300 K (x = 0, x = 0.75 and x = 0.9, respectively). (d)–(f) The corrected intensity *vs.* inverse temperature graphs fitted using an Arrhenius function for samples $Cs_2AgIn_xBi_{(1-x)}Cl_6$ (x = 0, x = 0.75, and x = 0.90), respectively. (g)–(i) The $(FWHM)^2$ *vs.* $(1/T)$ graphs for $Cs_2AgIn_xBi_{(1-x)}Cl_6$ (x = 0, x = 0.75, and x = 0.90), respectively.

temperature T and 0 K, respectively, A is a constant, k_B is the Boltzmann constant, and E_a is the activation energy. The extracted activation energy values are provided in Table S5 of the SI. The minimum activation energy for the $Cs_2AgIn_xBi_{(1-x)}Cl_6$ (x = 0.9) sample indicates a significant reduction in non-radiative recombination, thereby confirming the enhanced optical performance of the sample. The decreased intensity is associated with the peak broadening and attributed to phonon-mediated self-trapped excitonic recombination. The change in intensity is attributed to the trapping and detrapping of excitons through thermally activated STE states. To study the effect of exciton–phonon coupling, the temperature dependence of peak broadening is examined using the following equation:

$$\mathrm{FWHM} = 2.36\sqrt{S}\hbar\omega_{\mathrm{phonon}}\sqrt{\coth\frac{\hbar\omega_{\mathrm{phonon}}}{2k_BT}} \quad (10)$$

where $\hbar\omega_{\mathrm{phonon}}$ is the phonon energy and S is the Huang–Rhys factor, which represents the strength of the exciton–phonon coupling in the material. By fitting the temperature-dependent FWHM broadening, the values of the Huang–Rhys factor and optical phonon energy were determined. The calculated values of S and $\hbar\omega_{\mathrm{phonon}}$, along with the corresponding R^2 values, are shown in Table S5 of the SI. Here, $Cs_2AgIn_xBi_{(1-x)}Cl_6$ (x = 0.9) exhibits the lowest value of S, indicating a reduction in the strength of the exciton–phonon coupling upon In incorporation. Moreover, the S value is moderate for all samples, as shown in Table S5, which can balance the exciton–phonon coupling in the material. The deconvoluted TDPL spectra of $Cs_2AgIn_xBi_{(1-x)}Cl_6$ (x = 0, 0.75, 0.9) are shown in Fig. S17 of the SI. The details are provided in the SI.

3.5 Photodetector measurements

Fig. 6 displays the current–voltage (I–V) characteristics of $Cs_2AgIn_xBi_{(1-x)}Cl_6$ films under dark and white light illumination conditions. The I–V characteristics of films with a voltage sweep in the range of −1.0 V to +1.0 V are shown in Fig. 6(a), (d) and (g). The non-linear behavior of all I–V curves confirms the formation of a Schottky contact. The photoresponse of the films was measured under alternating dark and white light illumination (30 mW cm^{-2}) at zero bias voltage at room temperature. When light is incident on the device, the absorber material (perovskite layer) absorbs photons, generating electron–hole

Open Access Article. Published on 04 September 2025. Downloaded on 1/29/2026 4:49:33 AM.
This article is licensed under a Creative Commons Attribution 3.0 Unported Licence.

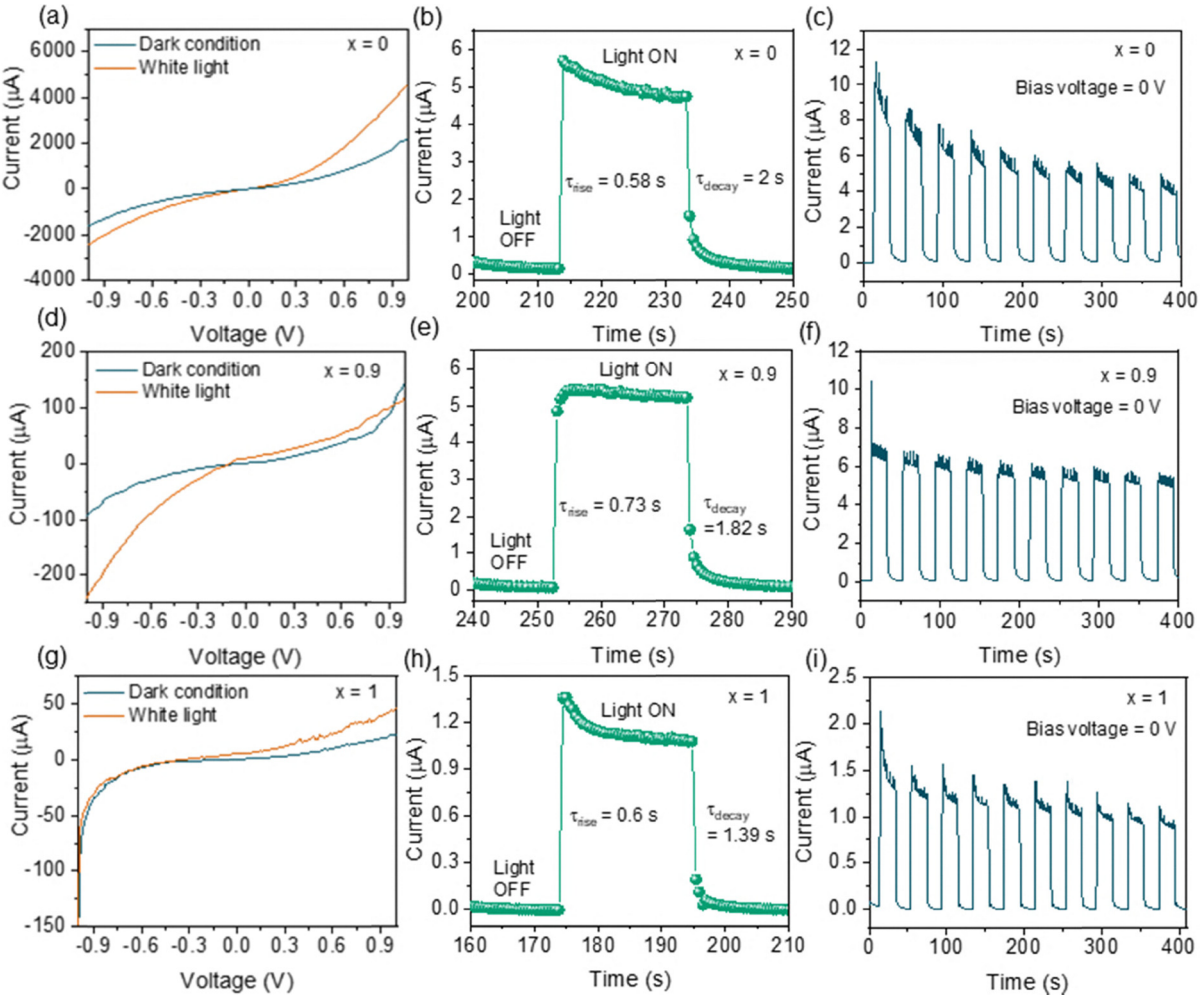

Fig. 6 $Cs_2AgIn_xBi_{(1-x)}Cl_6$ double perovskite-based photodetector device characteristics. (a), (d) and (g) *I–V* characteristics of $Cs_2AgIn_xBi_{(1-x)}Cl_6$ (x = 0, 0.9, 1) under white light illumination and dark conditions; (b), (e) and (h) current *versus* time plots under dark and white light illumination conditions for $Cs_2AgIn_xBi_{(1-x)}Cl_6$ (x = 0, 0.9, 1); and (c), (f) and (i) current *versus* time single-cycle plots of $Cs_2AgIn_xBi_{(1-x)}Cl_6$ (x = 0, 0.9, 1), respectively.

pairs (excitons). The electrons are selectively extracted by the TiO_2 layer and move towards the FTO, leaving behind the holes. The electrons then flow through the external circuit to the graphite electrode, where they recombine with the holes, completing the circuit and generating a photocurrent. To evaluate the response of the devices, the light source is switched on and off at 20 s intervals. The photoresponse measured for the three devices for 10 cycles is shown in Fig. 6(c), (f) and (i). At zero bias, all the devices show current in the μA range. Among the three materials, $Cs_2AgIn_xBi_{(1-x)}Cl_6$ (x = 0.9) exhibits the highest photocurrent and maintains excellent photocurrent stability over time, without a reduction in photocurrent. This implies that the device based on the $Cs_2AgIn_xBi_{(1-x)}Cl_6$ (x = 0.90) absorber material can show excellent photovoltaic performance with good stability.

It shows a constant current during cycling, indicating its good stability and repeatability. The high value of current may be attributed to its high absorption coefficient and reduced defect states, as evidenced by the optical properties. Also, the reduced trap states reduce the recombination of charge carriers, increasing the photocurrent. The performance of photodetectors is characterized by various parameters, including photoresponsivity and detectivity. The photoexcited current generated per unit power of incident light on the effective area of a photodetector is called photoresponsivity[60] and is calculated by

$$R_\lambda = \frac{\Delta I}{P_\lambda \times A}, \tag{11}$$

where $I = I_{photo} - I_{dark}$ is the change in photocurrent due to light incident on the effective photo-sensing area, P_λ is the intensity of incident light (30 mW cm^{-2}), and A' is the active area of the film (1.5 × 1.5 cm^2). For photodetectors, detectivity (D^*) measures the quality of the detector. It is measured in Jones and is expressed as:[61]

$$D^* = \frac{R_\lambda}{(2e \times J_{dark})^{1/2}} \tag{12}$$

where J_{dark} is the dark current density and e is the electron charge. The values of photoresponsivity and detectivity

 This journal is © the Owner Societies 2025

Open Access Article. Published on 04 September 2025. Downloaded on 1/29/2026 4:49:33 AM. This article is licensed under a Creative Commons Attribution 3.0 Unported Licence.

extracted from the obtained data are provided in Table S6 of the SI. As evidenced by the results, the responsivity and detectivity values extracted are maximum for the $Cs_2AgIn_xBi_{(1-x)}Cl_6$ (x = 0.9) sample, indicating improved optoelectronic performance. The rise time (τ_{rise}) is defined as the time needed for a photodetector to change from 10% to 90% of its maximum photocurrent from its dark current value. Likewise, the decay time (τ_{decay}) is the time required for the photodetector to decrease from 90% to 10% of its minimum dark current value, starting from its photocurrent value. A single photoresponse cycle was analyzed, and the rise (τ_r) and decay times (τ_d) were estimated from it. The rise and decay times calculated for all three samples are presented in Table S6 of the SI. Table S7 of the SI summarizes the reported device architectures and the key parameters of perovskite photodetectors. The table compares our results with representative values reported for lead halide perovskites and other DPs in recent literature.

4. Conclusions

In summary, we have successfully synthesized cubic-phase $Cs_2AgIn_xBi_{(1-x)}Cl_6$ materials by the antisolvent recrystallization method. EDS compositional analysis demonstrates the successful incorporation and homogeneous distribution of In into the $Cs_2AgBiCl_6$ framework. Complementary first-principles DFT calculations confirm the transition from indirect band gap $Cs_2AgIn_xBi_{(1-x)}Cl_6$ (x = 0) to direct band gap $Cs_2AgIn_xBi_{(1-x)}Cl_6$ (x = 1) at the Γ-point in the Brillouin zone. Absorption spectra indicate a long tail towards higher wavelengths, suggesting that the sub-bandgap state transition could arise from the trap states. PL measurements reveal a drastic increase in intensity above 75% In concentration with dual emission, whereas the TRPL results show an increase in average lifetime values with an increase in In content, suggesting that the materials have excellent optical properties and are hence suitable candidates for optoelectronics. The TDPL results yield a moderate value of the Huang–Rhys factor, which can balance the exciton–phonon coupling, leading to high PLQY values. The optimized lattice parameters and band gap values calculated from DFT analysis closely match the experimental values. The photodetector measurements of $Cs_2AgIn_xBi_{(1-x)}Cl_6$ (x = 0.90) films reveal a responsivity of ∼0.08 mA W^{-1} and a good detectivity of ∼63.5 × 10^{10} Jones at a voltage bias of 0 V. These findings pave the way for lead-free, highly stable, and self-biased photodetectors based on $Cs_2AgIn_xBi_{1-x}Cl_6$ double perovskites.

Conflicts of interest

There are no conflicts of interest to declare.

Data availability

The authors confirm that the data supporting the findings of this study are available within the article and/or its SI. Supplementary information: Fig. S1 (a) W–H plot for the $Cs_2AgIn_xBi_{(1-x)}Cl_6$ (x = 0.0) sample; (b) W–H plot for the $Cs_2AgIn_xBi_{(1-x)}Cl_6$ (x = 0.25) sample; (c) W–H plot for the $Cs_2AgIn_xBi_{(1-x)}Cl_6$ (x = 0.50) sample; (d) W–H plot for the $Cs_2AgIn_xBi_{(1-x)}Cl_6$ (x = 0.75) sample; (e) W–H plot for the $Cs_2AgIn_xBi_{(1-x)}Cl_6$ (x = 0.90) sample; (f) W–H plot for the $Cs_2AgIn_xBi_{(1-x)}Cl_6$ (x = 1) sample. Fig. S2 (a) Low-resolution TEM image and (b) histogram of $Cs_2AgIn_xBi_{(1-xa)}Cl_6$ (x = 0), (c) TEM image and (d) histogram of $Cs_2AgIn_xBi_{(1-x)}Cl_6$ (x = 1). Fig. S3 (a)–(c) HR-TEM images of $Cs_2AgIn_xBi_{(1-x)}Cl_6$ (x = 0.0, x = 0.50, and x = 0.75) samples, respectively. (d)–(f) SAED patterns of $Cs_2AgIn_xBi_{(1-x)}Cl_6$ (x = 0.0, x = 0.50 and x = 0.75) samples, respectively. Fig. S4 FE-SEM images of $Cs_2AgIn_xBi_{(1-x)}Cl_6$ (x = 0.50 (a), x = 0.75 (b), x = 0.90 (c), and x = 1.0 (d)) samples, respectively, at the 200 nm scale. Fig. S5 EDS spectra of the synthesized samples in the energy range 0–15 keV. Fig. S6–S10 Elemental mapping of $Cs_2AgIn_xBi_{(1-x)}Cl_6$ (x = 0.0, x = 0.50, x = 0.75, x = 0.90 and x = 1.0) samples, respectively. Fig. S11 (a1)–(a5) Core level XPS spectra of the $Cs_2AgIn_xBi_{(1-x)}Cl_6$ (x = 0.1) sample. (b1)–(b5) Core level XPS spectra of the x = 0.25 sample. (c1)–(c5) Core level XPS spectra of $Cs_2AgIn_xBi_{(1-x)}Cl_6$ (x = 0.9) sample. Fig. S12 (a1)–(a5) Survey scan XPS spectra of $Cs_2AgIn_xBi_{(1-x)}Cl_6$ (x =0.10, x = 0.25, x = 0.50, x = 0.75 and x = 0.90) samples, respectively. (b1) Survey scan XPS spectra of the $Cs_2AgIn_xBi_{(1-x)}Cl6$ (x = 1) sample. (b2)–(b5) Core level XPS spectra at 100× magnification. Fig. S13 Pseudo-absorption spectra of $Cs_2AgIn_xBi_{(1-x)}Cl_6$. Fig. S14 Fitted TRPL curves; Fig. S15 Comparison of optical and electrochemical band gaps estimated from UV and CV, respectively. Fig. S16 (a)–(c) The TDPL spectra of $Cs_2AgIn_xBi_{(1-x)}Cl_6$ (x = 0.25, x = 0.5 and x = 1.0 samples, respectively) recorded in the temperature range 80 K–300 K. (d)–(f) The corrected intensity *vs.* inverse temperature graphs fitted using an Arrhenius function for the x = 0.25, x = 0.5 and x = 1.0 samples, respectively. (g)–(i) The $(FWHM)^2$ *vs.* $1/T$ graphs for the x = 0.25, x = 0.50, and x = 1.0 samples, respectively. Fig. S17 (a)–(c) Deconvoluted temperature-dependent photoluminescence (TDPL) spectra of $Cs_2AgIn_xBi_{(1-x)}Cl_6$ (x = 0) at different temperatures. (d)–(f) Deconvoluted TDPL spectra of $Cs_2AgIn_xBi_{(1-x)}Cl_6$ (x = 0.75) at different temperatures. (g)–(i) Deconvoluted TDPL spectra of $Cs_2AgIn_xBi_{(1-x)}Cl_6$ (x = 0.9) at different temperatures. Fig. S18 (a) Photoluminescence excitation (PLE) spectrum of the x = 0 sample; (b) and (c) the photoluminescence excitation (PLE) spectra of the x = 0.75 sample corresponding to emissions in the violet and yellow regions, respectively; (d) and (e) the photoluminescence excitation (PLE) spectra of the x = 0.90 sample corresponding to emissions in the violet and orange regions, respectively; (f) the low temperature PLE spectra for the x = 1.0 sample. Table S1: comparison between the structural parameters calculated from XRD by Scherrer and W–H analyses. Table S2: optical band gap values estimated from UV-visible diffuse reflectance spectroscopy (DRS). Table S3: atomic percentages of elements calculated from EDS analysis. Table S4: TRPL traces recorded for emission in the violet/blue region for x = 0.75 and x = 0.90 samples, respectively. Table S5: the values of activation energy (E_a), the Huang–Rhys parameter (S), phonon energy, and the corresponding values of R^2 obtained

Open Access Article. Published on 04 September 2025. Downloaded on 1/29/2026 4:49:33 AM. This article is licensed under a Creative Commons Attribution 3.0 Unported Licence.

from fitted curves. Table S6: photoresponse parameters calculated for the photodetectors based on $Cs_2AgIn_xBi_{(1-x)}Cl_6$ (x = 0.0, 0.9, 1.0) under white light illumination. Table S7: summary of the reported device architectures and important parameters of perovskite photodetectors, comparing our results with representative values reported for lead halide perovskites and other DPs in recent literature. See DOI: https://doi.org/10.1039/d5cp02259b.

The raw data are available from the corresponding author (NYD) on request.

Acknowledgements

SNR expresses gratitude to the Chhatrapati Shahu Maharaj Research Training and Human Development Institute (SARTHI) for their generous financial assistance. GKR acknowledges the Manipal Academy of Higher Education for providing Dr TMA Pai Scholarship. MPN is grateful for the Seed Money scheme offered by Reva University. YJ is thankful to the BacPlex Technologies Private Limited, AIC Seed Foundation, Indian Institute of Science Education and Research (IISER) Pune for providing the laboratory facilities. NYD acknowledges the U.S. Department of Energy funding (DE-SC0025350) and the Penn State Institute for Computational and Data Sciences (ICDS) seed grant support. The computational aspects of this research were carried out utilizing the computing resources of the Roar supercomputer at the Institute for Computational and Data Sciences, Pennsylvania State University.

References

1 A. D. Jodlowski, C. Roldán-Carmona, G. Grancini, M. Salado, M. Ralaiarisoa, S. Ahmad, N. Koch, L. Camacho, G. de Miguel and M. K. Nazeeruddin, Large Guanidinium Cation Mixed with Methylammonium in Lead Iodide Perovskites for 19% Efficient Solar Cells, *Nat. Energy*, 2017, **2**(12), 972–979, DOI: 10.1038/s41560-017-0054-3.

2 G. Li, F. W. R. Rivarola, N. J. L. K. Davis, S. Bai, T. C. Jellicoe, F. de la Peña, S. Hou, C. Ducati, F. Gao, R. H. Friend, N. C. Greenham and Z. Tan, Highly Efficient Perovskite Nanocrystal Light-Emitting Diodes Enabled by a Universal Crosslinking Method, *Adv. Mater.*, 2016, **28**(18), 3528–3534, DOI: 10.1002/adma.201600064.

3 Y. Gao, C. Huang, C. Hao, S. Sun, L. Zhang, C. Zhang, Z. Duan, K. Wang, Z. Jin, N. Zhang, A. V. Kildishev, C.-W. Qiu, Q. Song and S. Xiao, Lead Halide Perovskite Nanostructures for Dynamic Color Display, *ACS Nano*, 2018, **12**(9), 8847–8854, DOI: 10.1021/acsnano.8b02425.

4 D. Amgar, A. Stern, D. Rotem, D. Porath and L. Etgar, Tunable Length and Optical Properties of CsPbX 3 (X = Cl, Br, I) Nanowires with a Few Unit Cells, *Nano Lett.*, 2017, **17**(2), 1007–1013, DOI: 10.1021/acs.nanolett.6b04381.

5 J. Lin, L. Gomez, C. de Weerd, Y. Fujiwara, T. Gregorkiewicz and K. Suenaga, Direct Observation of Band Structure Modifications in Nanocrystals of CsPbBr 3 Perovskite, *Nano Lett.*, 2016, **16**(11), 7198–7202, DOI: 10.1021/acs.nanolett.6b03552.

6 J. Zhou, X. Rong, M. S. Molokeev, X. Zhang and Z. Xia, Exploring the Transposition Effects on the Electronic and Optical Properties of $Cs_2AgSbCl_6$ via a Combined Computational-Experimental Approach, *J. Mater. Chem. A*, 2018, **6**(5), 2346–2352, DOI: 10.1039/C7TA10062K.

7 J. De Roo, M. Ibáñez, P. Geiregat, G. Nedelcu, W. Walravens, J. Maes, J. C. Martins, I. Van Driessche, M. V. Kovalenko and Z. Hens, Highly Dynamic Ligand Binding and Light Absorption Coefficient of Cesium Lead Bromide Perovskite Nanocrystals, *ACS Nano*, 2016, **10**(2), 2071–2081, DOI: 10.1021/acsnano.5b06295.

8 I. L. Braly, D. W. DeQuilettes, L. M. Pazos-Outón, S. Burke, M. E. Ziffer, D. S. Ginger and H. W. Hillhouse, Hybrid Perovskite Films Approaching the Radiative Limit with over 90% Photoluminescence Quantum Efficiency, *Nat. Photonics*, 2018, **12**(6), 355–361, DOI: 10.1038/s41566-018-0154-z.

9 G. Nedelcu, L. Protesescu, S. Yakunin, M. I. Bodnarchuk, M. J. Grotevent and M. V. Kovalenko, Fast Anion-Exchange in Highly Luminescent Nanocrystals of Cesium Lead Halide Perovskites ($CsPbX_3$, X = Cl, Br, I), *Nano Lett.*, 2015, **15**(8), 5635–5640, DOI: 10.1021/acs.nanolett.5b02404.

10 K. Du, W. Meng, X. Wang, Y. Yan and D. B. Mitzi, Bandgap Engineering of Lead-Free Double Perovskite Cs 2 AgBiBr 6 through Trivalent Metal Alloying, *Angew. Chem., Int. Ed.*, 2017, **56**(28), 8158–8162, DOI: 10.1002/anie.201703970.

11 Y. Bi, E. M. Hutter, Y. Fang, Q. Dong, J. Huang and T. J. Savenije, Charge Carrier Lifetimes Exceeding 15 Ms in Methylammonium Lead Iodide Single Crystals, *J. Phys. Chem. Lett.*, 2016, **7**(5), 923–928, DOI: 10.1021/acs.jpclett.6b00269.

12 Q. Dong, Y. Fang, Y. Shao, P. Mulligan, J. Qiu, L. Cao and J. Huang, Electron-Hole Diffusion Lengths > 175 Mm in Solution-Grown $CH_3NH_3PbI_3$ Single Crystals, *Science*, 2015, **347**(6225), 967–970, DOI: 10.1126/science.aaa5760.

13 L. Etgar, The Merit of Perovskite's Dimensionality; Can This Replace the 3D Halide Perovskite?, *Energy Environ. Sci.*, 2018, **11**(2), 234–242, DOI: 10.1039/C7EE03397D.

14 F. Wang, X. Jiang, H. Chen, Y. Shang, H. Liu, J. Wei, W. Zhou, H. He, W. Liu and Z. Ning, 2D-Quasi-2D-3D Hierarchy Structure for Tin Perovskite Solar Cells with Enhanced Efficiency and Stability, *Joule*, 2018, **2**(12), 2732–2743, DOI: 10.1016/j.joule.2018.09.012.

15 A. Krishna, S. Gottis, M. K. Nazeeruddin and F. Sauvage, Mixed Dimensional 2D/3D Hybrid Perovskite Absorbers: The Future of Perovskite Solar Cells?, *Adv. Funct. Mater.*, 2019, **29**(8), 1806482, DOI: 10.1002/adfm.201806482.

16 G. H. Murtaza and I. Ahmad, First principle study of the structural and optoelectronic properties of cubic perovskites CsPbM3 (M= Cl, Br, I), *Phys. B*, 2011, **406**(17), 3222–3229, DOI: 10.1016/j.physb.2011.05.028.

17 S. Yakunin, L. Protesescu, F. Krieg, M. I. Bodnarchuk, G. Nedelcu, M. Humer, G. De Luca, M. Fiebig, W. Heiss and M. V. Kovalenko, Low-threshold amplified spontaneous emission and lasing from colloidal nanocrystals of caesium

Open Access Article. Published on 04 September 2025. Downloaded on 1/29/2026 4:49:33 AM. This article is licensed under a Creative Commons Attribution 3.0 Unported Licence.

lead halide perovskites, *Nat. Commun.*, 2015, **6**(1), 8056, DOI: 10.1038/ncomms9056.

18 L. Protesescu, S. Yakunin, M. I. Bodnarchuk, F. Krieg, R. Caputo, C. H. Hendon, R. X. Yang, A. Walsh and M. V. Kovalenko, Nanocrystals of Cesium Lead Halide Perovskites ($CsPbX_3$, X = Cl, Br, and I): Novel Optoelectronic Materials Showing Bright Emission with Wide Color Gamut, *Nano Lett.*, 2015, **15**(6), 3692–3696, DOI: 10.1021/nl5048779.

19 E. M. Hutter, M. C. Gélvez-Rueda, A. Osherov, V. Bulović, F. C. Grozema, S. D. Stranks and T. J. Savenije, Direct–Indirect Character of the Bandgap in Methylammonium Lead Iodide Perovskite, *Nat. Mater.*, 2017, **16**(1), 115–120, DOI: 10.1038/nmat4765.

20 B. Park, B. Philippe, X. Zhang, H. Rensmo, G. Boschloo and E. M. J. Johansson, Bismuth Based Hybrid Perovskites $A_3Bi_2I_9$ (A: Methylammonium or Cesium) for Solar Cell Application, *Adv. Mater.*, 2015, **27**(43), 6806–6813, DOI: 10.1002/adma.201501978.

21 J.-C. Hebig, I. Kühn, J. Flohre and T. Kirchartz, Optoelectronic Properties of $(CH_3NH_3)_3$ Sb_2I_9 Thin Films for Photovoltaic Applications, *ACS Energy Lett.*, 2016, **1**(1), 309–314, DOI: 10.1021/acsenergylett.6b00170.

22 A. H. Slavney, T. Hu, A. M. Lindenberg and H. I. Karunadasa, A Bismuth-Halide Double Perovskite with Long Carrier Recombination Lifetime for Photovoltaic Applications, *J. Am. Chem. Soc.*, 2016, **138**(7), 2138–2141, DOI: 10.1021/jacs.5b13294.

23 E. T. McClure, M. R. Ball, W. Windl and P. M. Woodward, Cs_2AgBiX_6 (X = Br, Cl): New Visible Light Absorbing, Lead-Free Halide Perovskite Semiconductors, *Chem. Mater.*, 2016, **28**(5), 1348–1354, DOI: 10.1021/acs.chemmater.5b04231.

24 M. Leng, Z. Chen, Y. Yang, Z. Li, K. Zeng, K. Li, G. Niu, Y. He, Q. Zhou and J. Tang, Lead-Free, Blue Emitting Bismuth Halide Perovskite Quantum Dots, *Angew. Chem., Int. Ed.*, 2016, **55**(48), 15012–15016, DOI: 10.1002/anie.201608160.

25 B. Yang, J. Chen, F. Hong, X. Mao, K. Zheng, S. Yang, Y. Li, T. Pullerits, W. Deng and K. Han, Lead-Free, Air-Stable All-Inorganic Cesium Bismuth Halide Perovskite Nanocrystals, *Angew. Chem., Int. Ed.*, 2017, **56**(41), 12471–12475, DOI: 10.1002/anie.201704739.

26 J. Zhang, Y. Yang, H. Deng, U. Farooq, X. Yang, J. Khan, J. Tang and H. Song, High Quantum Yield Blue Emission from Lead-Free Inorganic Antimony Halide Perovskite Colloidal Quantum Dots, *ACS Nano*, 2017, **11**(9), 9294–9302, DOI: 10.1021/acsnano.7b04683.

27 Y. Zhang, J. Yin, M. R. Parida, G. H. Ahmed, J. Pan, O. M. Bakr, J.-L. Brédas and O. F. Mohammed, Direct-Indirect Nature of the Bandgap in Lead-Free Perovskite Nanocrystals, *J. Phys. Chem. Lett.*, 2017, **8**(14), 3173–3177, DOI: 10.1021/acs.jpclett.7b01381.

28 B. Yang, J. Chen, S. Yang, F. Hong, L. Sun, P. Han, T. Pullerits, W. Deng and K. Han, Lead-Free Silver-Bismuth Halide Double Perovskite Nanocrystals, *Angew. Chem., Int. Ed.*, 2018, **57**(19), 5359–5363, DOI: 10.1002/anie.201800660.

29 S. E. Creutz, E. N. Crites, M. C. De Siena and D. R. Gamelin, Colloidal Nanocrystals of Lead-Free Double-Perovskite (Elpasolite) Semiconductors: Synthesis and Anion Exchange To Access New Materials, *Nano Lett.*, 2018, **18**(2), 1118–1123, DOI: 10.1021/acs.nanolett.7b04659.

30 Y. Bekenstein, J. C. Dahl, J. Huang, W. T. Osowiecki, J. K. Swabeck, E. M. Chan, P. Yang and A. P. Alivisatos, The Making and Breaking of Lead-Free Double Perovskite Nanocrystals of Cesium Silver–Bismuth Halide Compositions, *Nano Lett.*, 2018, **18**(6), 3502–3508, DOI: 10.1021/acs.nanolett.8b00560.

31 J. Luo, S. Li, H. Wu, Y. Zhou, Y. Li, J. Liu, J. Li, K. Li, F. Yi, G. Niu and J. Tang, $Cs_2AgInCl_6$ Double Perovskite Single Crystals: Parity Forbidden Transitions and Their Application For Sensitive and Fast UV Photodetectors, *ACS Photonics*, 2018, **5**(2), 398–405, DOI: 10.1021/acsphotonics.7b00837.

32 G. Volonakis, A. A. Haghighirad, R. L. Milot, W. H. Sio, M. R. Filip, B. Wenger, M. B. Johnston, L. M. Herz, H. J. Snaith and F. Giustino, Cs 2 InAgCl 6: A New Lead-Free Halide Double Perovskite with Direct Band Gap, *J. Phys. Chem. Lett.*, 2017, **8**(4), 772–778, DOI: 10.1021/acs.jpclett.6b02682.

33 B. Yang, X. Mao, F. Hong, W. Meng, Y. Tang, X. Xia, S. Yang, W. Deng and K. Han, Lead-Free Direct Band Gap Double-Perovskite Nanocrystals with Bright Dual-Color Emission, *J. Am. Chem. Soc.*, 2018, **140**(49), 17001–17006, DOI: 10.1021/jacs.8b07424.

34 F. Locardi, M. Cirignano, D. Baranov, Z. Dang, M. Prato, F. Drago, M. Ferretti, V. Pinchetti, M. Fanciulli, S. Brovelli, L. De Trizio and L. Manna, Colloidal Synthesis of Double Perovskite $Cs_2AgInCl_6$ and Mn-Doped $Cs_2AgInCl_6$ Nanocrystals, *J. Am. Chem. Soc.*, 2018, **140**(40), 12989–12995, DOI: 10.1021/jacs.8b07983.

35 P. Zhang, J. Yang and S.-H. Wei, Manipulation of Cation Combinations and Configurations of Halide Double Perovskites for Solar Cell Absorbers, *J. Mater. Chem. A*, 2018, **6**(4), 1809–1815, DOI: 10.1039/C7TA09713A.

36 J. Luo, X. Wang, S. Li, J. Liu, Y. Guo, G. Niu, L. Yao, Y. Fu, L. Gao, Q. Dong, C. Zhao, M. Leng, F. Ma, W. Liang, L. Wang, S. Jin, J. Han, L. Zhang, J. Etheridge, J. Wang, Y. Yan, E. H. Sargent and J. Tang, Efficient and Stable Emission of Warm-White Light from Lead-Free Halide Double Perovskites, *Nature*, 2018, **563**(7732), 541–545, DOI: 10.1038/s41586-018-0691-0.

37 X.-G. Zhao, D. Yang, J.-C. Ren, Y. Sun, Z. Xiao and L. Zhang, Rational Design of Halide Double Perovskites for Optoelectronic Applications, *Joule*, 2018, **2**(9), 1662–1673, DOI: 10.1016/j.joule.2018.06.017.

38 V. K. Ravi, N. Singhal and A. Nag, Initiation and Future Prospects of Colloidal Metal Halide Double-Perovskite Nanocrystals: Cs_2AgBiX_6 (X = Cl, Br, I), *J. Mater. Chem. A*, 2018, **6**(44), 21666–21675, DOI: 10.1039/C8TA06126B.

39 S. N. Rahane, G. K. Rahane, A. Mandal, Y. Jadhav, A. Godha, A. Rokade, S. Shah, Y. Hase, A. Waghmare, N. G. Saykar, A. Roy, K. N. Salgaonkar, D. Dubal, S. K. Makineni,

Open Access Article. Published on 04 September 2025. Downloaded on 1/29/2026 4:49:33 AM. This article is licensed under a Creative Commons Attribution 3.0 Unported Licence.

N. Y. Dzade, S. R. Jadkar and S. R. Rondiya, Lead-Free $Cs_2AgBiCl_6$ Double Perovskite: Experimental and Theoretical Insights into the Self-Trapping for Optoelectronic Applications, *ACS Phys. Chem. Au*, 2024, **4**(5), 476–489, DOI: 10.1021/acsphyschemau.4c00008.

40 S. V. Barma, S. B. Jathar, Y.-T. Huang, Y. A. Jadhav, G. K. Rahane, A. V. Rokade, M. P. Nasane, S. N. Rahane, R. W. Cross, M. P. Suryawanshi, S. B. Jo, R. L. Z. Hoye, S. R. Jadkar, N. Y. Dzade and S. R. Rondiya, Synthesis and Interface Engineering in Heterojunctions of Tin-Selenide-Based Nanostructures for Photoelectrochemical Water Splitting, *ACS Appl. Nano Mater.*, 2024, **7**(2), 1986–1999, DOI: 10.1021/acsanm.3c05202.

41 S. S. Deshpande, N. G. Saykar, A. Mandal, S. Rahane, Y. A. Jadhav, M. Upadhyay Kahaly, G. N. Nagy, A. Shinde, S. Suresh and S. R. Rondiya, Unravelling Structural, Optical, and Band Alignment Properties of Mixed Pb–Sn Metal-Halide Quasi-2D Ruddlesden–Popper Perovskites, *Langmuir*, 2024, **40**(31), 16180–16189, DOI: 10.1021/acs.langmuir.4c01278.

42 Y. A. Jadhav, P. R. Thakur and S. K. Haram, Voltammetry Investigation on Copper Zinc Tin Sulphide/Selenide ($CZTS_xSe_{1-x}$) Alloy Nanocrystals: Estimation of Composition Dependent Band Edge Parameters, *Sol. Energy Mater. Sol. Cells*, 2016, **155**, 273–279, DOI: 10.1016/j.solmat.2016.06.030.

43 G. Kresse and J. Furthmüller, Efficiency of Ab-Initio Total Energy Calculations for Metals and Semiconductors Using a Plane-Wave Basis Set, *Comput. Mater. Sci.*, 1996, **6**(1), 15–50, DOI: 10.1016/0927-0256(96)00008-0.

44 J. P. Perdew, K. Burke and M. Ernzerhof, Generalized Gradient Approximation Made Simple, *Phys. Rev. Lett.*, 1996, **77**(18), 3865–3868, DOI: 10.1103/PhysRevLett.77.3865.

45 P. E. Blöchl, Projector Augmented-Wave Method, *Phys. Rev. B:Condens. Matter Mater. Phys.*, 1994, **50**(24), 17953–17979, DOI: 10.1103/PhysRevB.50.17953.

46 H. J. Monkhorst and J. D. Pack, Special Points for Brillouin-Zone Integrations, *Phys. Rev. B*, 1976, **13**(12), 5188–5192, DOI: 10.1103/PhysRevB.13.5188.

47 S. Grimme, J. Antony, S. Ehrlich and H. Krieg, A Consistent and Accurate Ab Initio Parametrization of Density Functional Dispersion Correction (DFT-D) for the 94 Elements H-Pu, *J. Chem. Phys.*, 2010, **132**(15), 154104, DOI: 10.1063/1.3382344.

48 A. M. Ganose, A. J. Jackson and D. O. Scanlon, Sumo: Command-Line Tools for Plotting and Analysis of Periodic Ab Initio Calculations, *J. Open Source Software*, 2018, **3**(28), 717, DOI: 10.21105/joss.00717.

49 V. Wang, N. Xu, J.-C. Liu, G. Tang and W.-T. Geng, VASPKIT: A User-Friendly Interface Facilitating High-Throughput Computing and Analysis Using VASP Code, *Comput. Phys. Commun.*, 2021, **267**, 108033, DOI: 10.1016/j.cpc.2021.108033.

50 M. Fox, *Optical properties of solids*, Oxford Press, 2002, DOI: 10.1119/1.1691372.

51 Z. Xiao, K. Z. Du, W. Meng, J. Wang, D. B. Mitzi and Y. Yan, Intrinsic Instability of $Cs_2In(I)M(III)X_6$ (M = Bi, Sb; X = Halogen) Double Perovskites: A Combined Density Functional Theory and Experimental Study, *J. Am. Chem. Soc.*, 2017, **139**(17), 6054–6057, DOI: 10.1021/jacs.7b02227.

52 J. Zhou, Z. Xia, M. S. Molokeev, X. Zhang, D. Peng and Q. Liu, Composition design, optical gap and stability investigations of lead-free halide double perovskite $Cs_2AgInCl_6$, *J. Mater. Chem. A*, 2017, **5**, 15031, DOI: 10.1039/c7ta04690a.

53 D. Manna, J. Kangsabanik, T. K. Das, D. Das, A. Alam and A. Yella, Lattice Dynamics and Electron–Phonon Coupling in Lead-Free $Cs_2AgIn_{1-x}Bi_xCl_6$ Double Perovskite Nanocrystals, *J. Phys. Chem. Lett.*, 2020, **11**(6), 2113–2120, DOI: 10.1021/acs.jpclett.0c00206.

54 H. Siddique, Z. Xu, X. Li, S. Saeed, W. Liang, X. Wang, C. Gao, R. Dai, Z. Wang and Z. Zhang, Anomalous Octahedron Distortion of Bi-Alloyed $Cs_2AgInCl_6$ Crystal via XRD, Raman, Huang–Rhys Factor, and Photoluminescence, *J. Phys. Chem. Lett.*, 2020, **11**(22), 9572–9578, DOI: 10.1021/acs.jpclett.0c02852.

55 R. Zeng, L. Zhang, Y. Xue, B. Ke, Z. Zhao, D. Huang, Q. Wei, W. Zhou and B. Zou, Highly Efficient Blue Emission from Self-Trapped Excitons in Stable Sb^{3+}-Doped $Cs_2NaInCl_6$ Double Perovskites, *J. Phys. Chem. Lett.*, 2020, **11**(6), 2053–2061, DOI: 10.1021/acs.jpclett.0c00330.

56 G. Volonakis, M. R. Filip, A. A. Haghighirad, N. Sakai, B. Wenger, H. J. Snaith and F. Giustino, Lead-Free Halide Double Perovskites via Heterovalent Substitution of Noble Metals, *J. Phys. Chem. Lett.*, 2016, **7**(7), 1254–1259, DOI: 10.1021/acs.jpclett.6b00376.

57 W. Meng, X. Wang, Z. Xiao, J. Wang, D. B. Mitzi and Y. Yan, Parity-Forbidden Transitions and Their Impact on the Optical Absorption Properties of Lead-Free Metal Halide Perovskites and Double Perovskites, *J. Phys. Chem. Lett.*, 2017, **8**(13), 2999–3007, DOI: 10.1021/acs.jpclett.7b01042.

58 S. N. Inamdar, P. P. Ingole and S. K. Haram, Determination of Band Structure Parameters and the Quasi-Particle Gap of CdSe Quantum Dots by Cyclic Voltammetry, *ChemPhysChem*, 2008, **9**(17), 2574–2579, DOI: 10.1002/cphc.200800482.

59 S. Wadhai, Y. Jadhav and P. Thakur, Synthesis of Metal-Free Phosphorus Doped Graphitic Carbon Nitride-P25 (TiO2) Composite: Characterization, Cyclic Voltammetry and Photocatalytic Hydrogen Evolution, *Sol. Energy Mater. Sol. Cells*, 2021, **223**, 110958, DOI: 10.1016/j.solmat.2021.110958.

60 P. K. Kannan, D. J. Late, H. Morgan and C. S. Rout, Recent developments in 2D layered inorganic nanomaterials for sensing, *Nanoscale*, 2015, **7**, 13293–13312, DOI: 10.1039/C5NR03633J.

61 L. Dou, Y. M. Yang, J. You, Z. Hong, W.-H. Chang, G. Li and Y. Yang, Solution-processed hybrid perovskite photodetectors with high detectivity, *Nat. Commun.*, 2014, **5**, 5404, DOI: 10.1038/ncomms6404.